J. Fluid Mech. (2014), vol. 748, pp. 457–487. © Cambridge University Press 2014
doi:10.1017/jfm.2014.188

An experimental investigation of the turbulent mixing transition in the Richtmyer–Meshkov instability

Christopher R. Weber[1,2,†], **Nicholas S. Haehn**[1,‡], **Jason G. Oakley**[1],
David A. Rothamer[1] and **Riccardo Bonazza**[1]

[1]University of Wisconsin, Madison, WI 53706, USA

[2]Lawrence Livermore National Laboratory, Livermore, CA 94550, USA

(Received 4 September 2013; revised 18 January 2014; accepted 2 April 2014;
first published online 1 May 2014)

The Richtmyer–Meshkov instability (RMI) is experimentally investigated in a vertical shock tube using a broadband initial condition imposed on an interface between a helium–acetone mixture and argon ($A \approx 0.7$). The interface is created without the use of a membrane by first setting up a flat, gravitationally stable stagnation plane, where the gases are injected from the ends of the shock tube and exit through horizontal slots at the interface location. Following this, the interface is perturbed by injecting gas within the plane of the interface. Perturbations form in the lower portion of this layer due to the shear between this injected stream and the surrounding gas. This shear layer serves as a statistically repeatable broadband initial condition to the RMI. The interface is accelerated by either a $M = 1.6$ or $M = 2.2$ planar shock wave, and the development of the ensuing mixing layer is investigated using planar laser-induced fluorescence (PLIF). The PLIF images are processed to reveal the light-gas mole fraction by accounting for laser absorption and laser-steering effects. The images suggest a transition to turbulent mixing occurring during the experiment. An analysis of the mole-fraction distribution confirms this transition, showing the gases begin to homogenize at later times. The scalar variance energy spectra exhibits a near $k^{-5/3}$ inertial range, providing further evidence for turbulent mixing. Measurements of the Batchelor and Taylor microscales are made from the mole-fraction images, giving $\sim$150 μm and 4 mm, respectively, by the latest times. The ratio of these scales implies an outer-scale Reynolds number of 6–7 $\times$ 10^4.

Key words: instability, turbulent mixing, turbulent transition

1. Introduction

A shock wave passing through an interface between two densities will deposit vorticity on interfacial perturbations. This interaction, known as the Richtmyer–Meshkov instability (RMI) (Richtmyer 1960; Meshkov 1970), leads to the unbounded growth of perturbations and can result in turbulent mixing. The RMI is akin to the Rayleigh–Taylor instability (RTI) (Rayleigh 1883; Taylor 1950), where a finite

---

[†] Email address for correspondence: weber30@llnl.gov

[‡] Present address: Intel Corporation, Chandler, AZ 85226, USA.

acceleration causes an interface to become unstable. These instabilities can lead to mixing of material interfaces in inertial confinement fusion capsules (Lindl *et al.* 2004), the formation of supernova remnants (Kane, Drake & Remington 1999) and enhanced fuel-oxidizer mixing in supersonic combustion (Marble, Hendricks & Zukoski 1987).

The RMI starts with baroclinic production of vorticity, where a misalignment of the pressure gradient, ∇p, at the shock front and the density gradient, $\nabla \rho$, at the interface will lead to vorticity (ω) production: $\mathrm{D}\omega/\mathrm{D}t = (\nabla \rho \times \nabla p)/\rho^2$. The perturbations grow linearly until their amplitudes become comparable to their wavelengths. The interface can develop into a turbulent mixing layer if the initial perturbation contains a broad range of scales and it is accelerated by a sufficiently strong shock.

Turbulent mixing requires a separation between the largest, energy-containing scales and the smallest, dissipative scales. The controlling length scales are the Liepmann–Taylor scale λ_L (related to the Taylor microscale) and the inner viscous scale λ_ν (related to the Kolmogorov scale) (Dimotakis 2000). The Liepmann–Taylor scale is effectively the smallest scale generated by the largest eddies, while the inner viscous scale is the scale where energy begins to be removed through viscous dissipation. Thus, when $\lambda_L > \lambda_\nu$, turbulent mixing is expected. In steady-state flows, these scales are related to the Reynolds number through

$$\lambda_L = 5\mathcal{L}Re^{-1/2} \tag{1.1}$$

$$\lambda_\nu = 50\mathcal{L}Re^{-3/4}, \tag{1.2}$$

where $\mathcal{L}$ is the largest scale of the flow, which implies a transition Reynolds number of $Re = 1\text{–}2 \times 10^4$.

For time-dependent flows such as the RMI, the Reynolds number can exceed the turbulent transition before the flow develops the scale separation necessary for turbulent mixing. Robey *et al.* (2003) considered the case where the interface starts as a discontinuity and therefore the Taylor microscale begins at zero. With the Taylor microscale growing with time as $\lambda_T \propto \sqrt{\nu t}$, eventually it surpasses the viscous scales, marking a transition to turbulence. In the experiments discussed here, a different scenario occurs: the Taylor and viscous scales start at finite values set by the initial condition. After the shock interaction, where additional energy is deposited in the layer, these scales evolve towards their fully developed values.

Previous works have observed evidence of turbulent mixing in shock tube experiments. In a shock-accelerated gas curtain, Rightley *et al.* (1999) identified a turbulent transition when the intensity histogram of planar post-shock images no longer showed a local peak of unmixed fluid. Vorobieff, Rightley & Benjamin (1998) and Vorobieff *et al.* (2003) used second-order structure functions on images from similar experiments to identify turbulent mixing. The power-law slope of the structure function at late times was analogous to a $k^{-5/3}$ spectrum in wavenumber space. Recent work by Balakumar *et al.* (2012) used simultaneous density and velocity measurements to study the turbulent behaviour after a second shock wave interacted with the layer. A shock wave interacting with a spherical density inhomogeneity (a bubble or cloud) will form a ring of vorticity which has been observed to turbulently strip mass from the sphere (Ranjan, Oakley & Bonazza 2011). For the single-interface RMI, Zhou, Robey & Buckingham (2003) found that the single-mode experiments of Jones & Jacobs (1997) and Collins & Jacobs (2002) approached the transition limit at the latest times of their highest Mach number experiment, where the vortex cores exhibited a chaotic structure. In an earlier subset of the present work

(Weber *et al.* 2012), the shock-induced mixing layer appeared to be transitioning to turbulent mixing at the latest observed time. For the present experiments, the shock tube test section was extended to observe the mixing layer after this transition. In addition, a higher Mach number campaign was undertaken for a point of comparison.

In the experiments presented here, evidence for a transition to turbulent mixing of the shock-accelerated mixing layer is inferred by a homogenization of the mole-fraction probability density functions (PDFs) and the emergence of an inertial range in the scalar energy spectra. The length scales are measured and found to separate with time. The largest scale, the overall thickness of the mixing layer, initially grows linearly, the smallest scale, the Batchelor scale, decreases in size, and the intermediate Taylor microscale remains nearly constant. Coincident with the inferred turbulent transition, the Taylor microscale and the Batchelor scale appear sufficiently separated to sustain an inertial range. The paper begins with a description of the experimental set-up, the initial condition and the image processing. The results section describes the structure of the mixing layer as it evolves in time. Length scales are extracted from the mixing layer using several methods and are finally used to estimate the Reynolds number.

2. Experimental set-up

The present experiments were performed at the Wisconsin Shock Tube Laboratory. The shock tube is 9.1 m tall and has a 25.4 cm × 25.4 cm internal cross-section. The 2.0 m driver section is separated from the rest of the shock tube by a steel diaphragm. Before each experiment, the driver section is pressurized to 85 % of the diaphragm rupture pressure. The remaining pressure is rapidly provided through two pneumatically driven, fast-opening valves. The rupture of the diaphragm releases a shock wave into the atmospheric pressure gas below. The distance between the diaphragm and the interface, 5.4 m, allows the shock wave to stabilize and become planar before interacting with the interface. Twelve piezoelectric pressure transducers mounted in the walls of the shock tube detect the shock waves and help calculate the strength of the shock waves and, indirectly, information about the gas composition. The bottom section of the shock tube contains ports for generating the interface and windows for planar imaging. Four window ports are used in the present work. The top-most window is positioned to view the initial condition and an early post-shock time. Lower windows allow for later-time visualization. These windows are made of fused silica and are 7.5 cm thick to withstand the dynamic loading by strong shock waves. The end wall of the shock tube contains a rectangular window to transmit the laser sheets used for flow visualization.

These experiments use a gas interface with a mixture of helium and acetone vapour ($6.0 \pm 0.8\,\%$ by volume) above and pure argon below, giving an Atwood number of $A = (\rho_2 - \rho_1)/(\rho_2 + \rho_1) = 0.7$. The flow of the helium–acetone mixture is split, routing a portion to the top of the shock tube and the remaining to the interface section. First, an initially flat interface is formed by flowing the helium–acetone mixture into the top of the shock tube and argon into the bottom. Excess gas is evacuated through slots in the shock tube wall at the interface location. These slots are connected to a pair of vacuum pumps, ensuring a rapid outflow of gas. This method to create a flat, membrane-less interface is similar to that developed for the University of Arizona shock tube (Jones & Jacobs 1997) and used previously at the University of Wisconsin (Motl *et al.* 2009).

The flat interface is perturbed by injecting the pure argon and the helium–acetone mixture horizontally through separate slots above and below the stagnation plane,

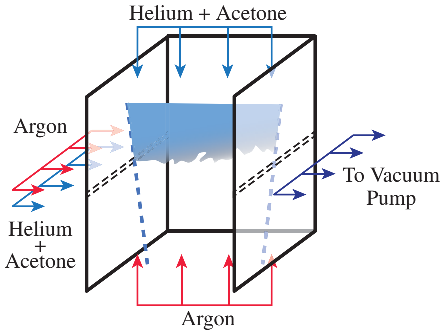

FIGURE 1. (Colour online) Diagram of the interface location showing gas flowing from the top and bottom of the shock tube and from the left set of slots. The right set of slots are connected to a vacuum pump, removing excess gas. The edges of the planar laser sheet are shown as dashed lines and the laser causes fluorescence in the acetone vapour in the top gas.

respectively, while maintaining the vertical flow started previously. This flow configuration, shown in figure 1, was experimentally determined to provide the best initial condition in terms of scale content and statistical repeatability. Perturbations form due to the buoyant interaction between the two streams and from the shear stress between this mixed layer and the pure argon. The superposition of the horizontal and vertical flows creates a continual flow towards the interface, ensuring that all mixed gas is removed and the mixing layer remains statistically steady in time.

Two excimer lasers (Lambda Physik LPX 210i, 308 nm, 470 mJ pulse^{-1}, 28 ns pulse) are used for planar laser-induced fluorescence (PLIF) diagnostics. During each experiment, 10 pre-shock images are recorded prior to the arrival of the shock wave to obtain a statistical description of the initial condition. To allow the laser to recharge and account for variability in experimental timing, the last recorded initial condition occurs 150–200 ms prior to the shock arriving at the interface. A pressure transducer above the interface is used to trigger the two lasers for two post-shock images. The images are all recorded using three thermoelectrically cooled (to $-60\,^{\circ}$C) Andor CCD cameras (model DV434-BU2).

The initial condition camera is set up with a resolution of 211 μm pixel^{-1}, while the post-shock cameras have 183 μm pixel^{-1} resolution. The imaging system resolution was measured using a scanning knife edge technique (Clemens 2002; Wang & Clemens 2004) with the optics and shock tube windows in place and found the standard deviation of the line spread function (σ_{LSF}) to be 151 μm for the post-shock cameras. The laser sheet was found to have a beam waist (occurring at the image centre) of 890 μm and an M-squared value of 75. The thickness of the laser sheet is rather large compared with the camera resolution and the smallest scales of the flow (discussed later), but measurements of the dissipation scales are less sensitive to laser sheet thickness than optical resolution. Kaiser & Frank (2011) find that the laser sheet can be approximately 5× larger than the imaging resolution and still have equivalent resolution in planar imaging of dissipation structures. The effects of laser sheet thickness on the measured spectra were estimated using synthetic turbulent images and are expected to overestimate the Batchelor scale by 10 %. No motion blur is expected in the post-shock images due to the short laser pulse (28 ns), rapid fluorescence emission (∼2 ns), and negligible phosphorescence at these high

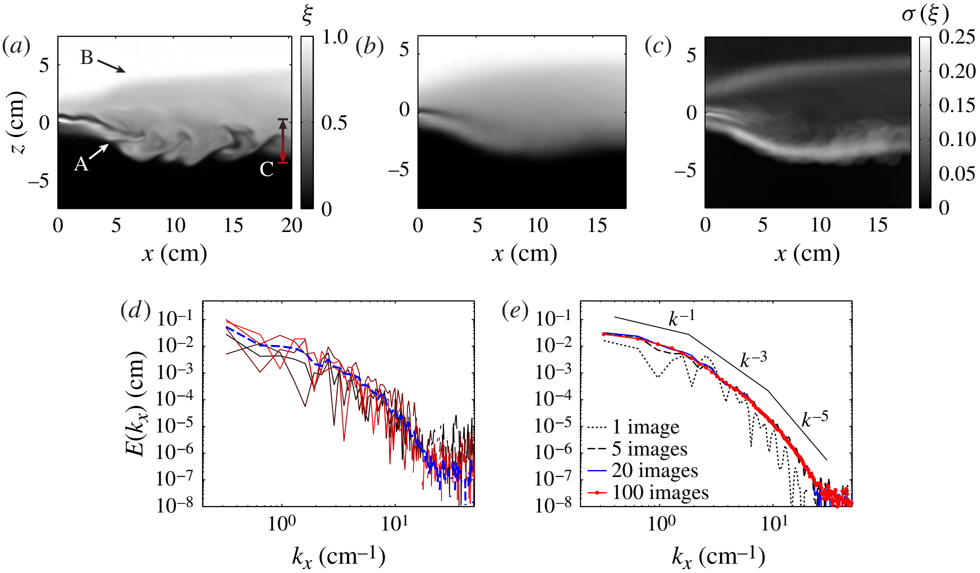

FIGURE 2. (Colour online) Initial condition characterization. (*a*) A sample initial condition image, processed so intensity corresponds to light-gas mole fraction. (*b*) Mole fraction ensemble average and (*c*) standard deviation, σ, from 100 images. (*d*) The scalar variance energy spectrum from several rows within region C of (*a*). The colour of the curves are related to the region C arrow. The average spectrum from this region is shown as a thick dashed line. (*e*) The ensemble-averaged spectrum within the $0.2 < \langle \xi \rangle < 0.3$ region.

temperatures. In the initial condition images, phosphorescence, with a ∼200 µs lifetime, introduces a blur of approximately 1 pixel.

Figure 2(*a*) shows a sample initial condition image, corrected so that the signal intensity corresponds to acetone concentration, which is also directly proportional to the light-gas mole fraction, ξ. In the image, the gases are injected from the left near $z = 0$ cm. The injected stream of pure argon ($\xi = 0$) is visible as a dark horizontal band at $z \approx 0.5$ cm. The injected helium–acetone mixture ($\xi = 1$) is visible below the argon stream. Approximately 5 cm to the right of the injection location (feature A), the two gas streams begin mixing and the individual streams are no longer apparent. Perturbations develop on the lower edge of this mixing region due to the velocity difference of the mixture stream and the ambient argon. The boundary between the mixed gas entering from the left and the helium–acetone mixture entering from the top of the shock tube is identified as feature B. The gradient at the top of the mixing region is diffuse and lacks noticeable perturbations. Between the top contour (feature B) and the bottom shear surface (feature A), the average mole fraction is $\xi \approx 0.6$. The ensemble average and standard deviation from 100 images are shown in figure 2(*b*,*c*). The most significant temporal fluctuations occur at the bottom shear surface, where the light-gas mole fraction has a standard deviation of 0.2. The scalar variance energy spectra from the initial condition are shown in figure 2(*d*,*e*). The spectra in figure 2(*d*) are taken from individual rows in region C of figure 2(*a*). These rows have average mole fraction values ranging from $\langle \xi \rangle = 0.1$ to 0.6 and are spaced 0.75 cm apart. The spectra show the wide range of scales present in the initial condition, with a few dominant modes present in each row. These dominant modes are weakly correlated with other rows, such that over this region the average spectrum, shown as a thick dashed line, shows a smoother, broadband spectrum. Similarly, ensemble averaging over a narrow region, $0.2 < \langle \xi \rangle < 0.3$, produces a smooth spectrum that is converged by 20 images, shown in figure 2(*e*), and has an approximate spectral shape of

$$E \propto \begin{cases} k^{-1} & k < 1.8\ \mathrm{cm}^{-1} \\ k^{-3} & 1.8\ \mathrm{cm}^{-1} \leqslant k \leqslant 9\ \mathrm{cm}^{-1} \\ k^{-5} & k > 9\ \mathrm{cm}^{-1}. \end{cases} \tag{2.1}$$

This initial condition is characterized further in Weber *et al.* (2012).

The interface is accelerated by an incident shock wave of strength $M_i = 1.57 \pm 0.02$ or $M_i = 2.23 \pm 0.02$. The incident shock wave speed, measured by pressure transducers in the helium–acetone mixture above the interface, is combined with the measured transmitted shock wave speed in the pure argon to determine the incident Mach number and the acetone composition of the light gas. This method of measuring the acetone composition agrees within 7 % of estimates made using Beer's law attenuation of laser light. As noted above, the interior of the initial condition layer has a mole fraction $\xi = 0.6$, thus it is useful to compute effective incident Mach numbers (the Mach number of the shock inside the $\xi = 0.6$ region) and an effective Atwood number between the $\xi = 0.6$ and $\xi = 0$ gas, giving $M_{ei} \approx 1.75$ or $M_{ei} = 2.62$ and $A_e \approx 0.32$. The shock will distort slightly as it transmits into this $\xi = 0.6$ region and take the shape of the perturbations identified as feature B in figure 2(*a*) due to differences in the incident wave speed in this region. This upper perturbation has an amplitude of ~1 cm over a width of 10 cm, producing a shock amplitude of 0.2–0.3 cm, or changing the shock angle by $<2^\circ$, i.e. a negligible amount compared with the large angle of the nonlinear perturbations at the bottom of the layer.

The PLIF images are processed to extract the light-gas mole fraction, ξ. The images are processed using the knowledge that the top portion of the image contains pure seeded (light) gas ($\xi = 1$). Integrating downward while accounting for the divergence of the laser sheet, deviations from Beer's law attenuation are attributed to mixing of unseeded (heavy) gas or changes in temperature. The equation for this is

$$\xi = \frac{(T/T_1)S_f}{S_{f,R} - n_1 \sigma \phi \int_r^R (S_f/\phi)\,\mathrm{d}r}, \tag{2.2}$$

where S_f is the local fluorescence signal, $S_{f,R}$ is the fluorescence signal at the top of the image where it is assumed $\xi = 1$, T/T_1 is the temperature ratio in relation to the pure seeded region, $n_1\sigma$ is the product of number density and absorption cross-section in the pure seeded gas (this product is measured by the exponential signal variation in the top of the image), and ϕ is the fluorescence quantum yield. The integral is carried out from the local location r to the top of the image at location R. This process (without the inclusion of temperature effects) is similar to that used by Collins & Jacobs (2002) and Motl *et al.* (2009). The temperature field is the result of the shock passing through a non-uniform medium and from mixing of materials at different temperatures. The interaction of a shock with continuous interface is already a non-trivial study (Chisnell 1955) and is complicated by the nonlinear effects of perturbations. Temperature equilibration due to mixing has a dependence on the specific heats of the different materials. Simulations of the shock-interface interaction (Weber 2012) and the correct relation due to mixing show a temperature–mole fraction dependence to within 3 % of linear. Therefore, the temperature is approximated as

$$T = T_2' + (T_1' - T_2')\xi, \tag{2.3}$$

M_i	1.57	2.23
M_t	1.85	2.88
W_i (m s^{-1})	1150	1576
W_t (m s^{-1})	592	919
V_0 (m s^{-1})	315	606
Acetone (% Vol.)	5.6	6.5
ρ_1 (kg m^{-3})	0.29	0.31
ρ_2 (kg m^{-3})	1.63	1.63
ρ_1' (kg m^{-3})	0.69	1.19
ρ_2' (kg m^{-3})	3.48	4.79
T_1' (K)	497	761
T_2' (K)	557	1011
$p_1' = p_2'$ (MPa)	0.40	1.01
A	0.70	0.68
A'	0.67	0.60
$(1 - V_0/W_i)$	0.73	0.62
$(\rho_1/\rho_1' + \rho_2/\rho_2')/2$	0.44	0.30

TABLE 1. Gas properties for the two Mach number cases. Primes denote post-shock quantities. Gas 1 is the light gas (helium seeded with acetone) and gas 2 is the heavy gas (argon). Here V_0 is the post-shock interface velocity.

where T_1' and T_2' are the post-shock temperatures in the pure light and heavy gases, respectively, calculated from 1D gas dynamics. With a Prandtl number near unity, this approximation is expected to remain first-order accurate throughout the experiment. Since the right-hand side of (2.2) contains ξ in the relation for T, $\sigma(T)$ and $\phi(T)$, this equation is iteratively solved until a converged mole fraction field is found. Once the images have been corrected, fine-scale features remain due to refraction of light rays caused by index of refraction gradients in the mixing layer. These features are clearly identified in 2D Fourier space as a narrow spectral-energy band in the k_x direction (Dimotakis, Catrakis & Fourguette 2001). This band (located within $|k_x| \geqslant 10.7$ cm^{-1} and $|k_z| \leqslant 1.79$ cm^{-1}) is replaced with spectral-energy values interpolated from outside this region at wavenumber $k = \sqrt{k_x^2 + k_z^2}$. The final corrected image, obtained by inverting the 2D notch-filtered spectrum, has these fine-scale artifacts greatly suppressed. This filtering process preserves the original spectrum when applied to synthetic turbulent images (Weber 2012).

At each Mach number, images from four post-shock times are obtained (termed PS1–PS4). These post-shock times correspond to different shock-tube window locations. Two post-shock images are obtained per experiment and a total of 20–40 images were collected at each time over the course of the experimental campaign. Some of the relevant gas properties are reported in table 1. These are computed based on the measured incident and transmitted wave speeds (W_i and W_t). Primes denote post-shock quantities.

3. Experimental results and discussion

3.1. *Structure of the post-shock scalar fields*

Figures 3 and 4 show a sample of corrected PLIF images from the $M = 1.6$ and $M = 2.2$ experiments, respectively. The laser sheet in the late-time location, near the end wall of the shock tube, is narrower than locations further from the end wall.

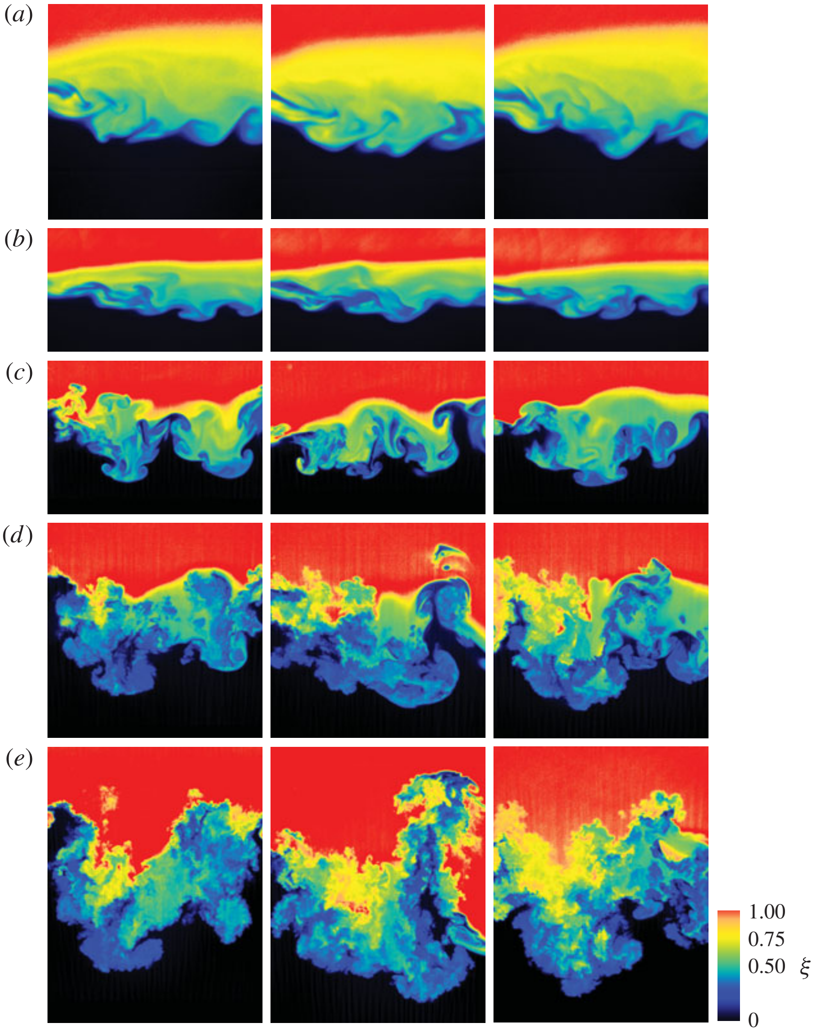

FIGURE 3. (Colour online) Selected images from $M = 1.6$ experimental sequence. First row: initial condition images. Second row: PS1, 0.14 ms after shock interaction. Third row: PS2, 0.88 ms after shock interaction. Fourth row: PS3, 2.16 ms after shock interaction. Fifth row: PS4, 3.84 ms after shock interaction. The width of each image is 14.0 cm.

Owing to this, all images in these figures are cropped to the PS4 width (14 cm). The first rows in each figure show three initial condition images. In figure 3 the second, third, fourth and fifth rows of images are at post-shock times of 0.14, 0.88, 2.16 and 3.84 ms, respectively. The post-shock times in figure 4 are 0.10, 0.44, 1.12 and 2.05 ms. Images in the same column in rows four and five are from the same experiment, whereas all other images are from different experiments.

The images show the large-scale extent of the mixing layer is growing, while the fluid within the layer is becoming more mixed and turbulent (to be quantified later). The earliest post-shock images seem to have features similar to those seen in the initial condition images, but the gradients are somewhat sharper due to the

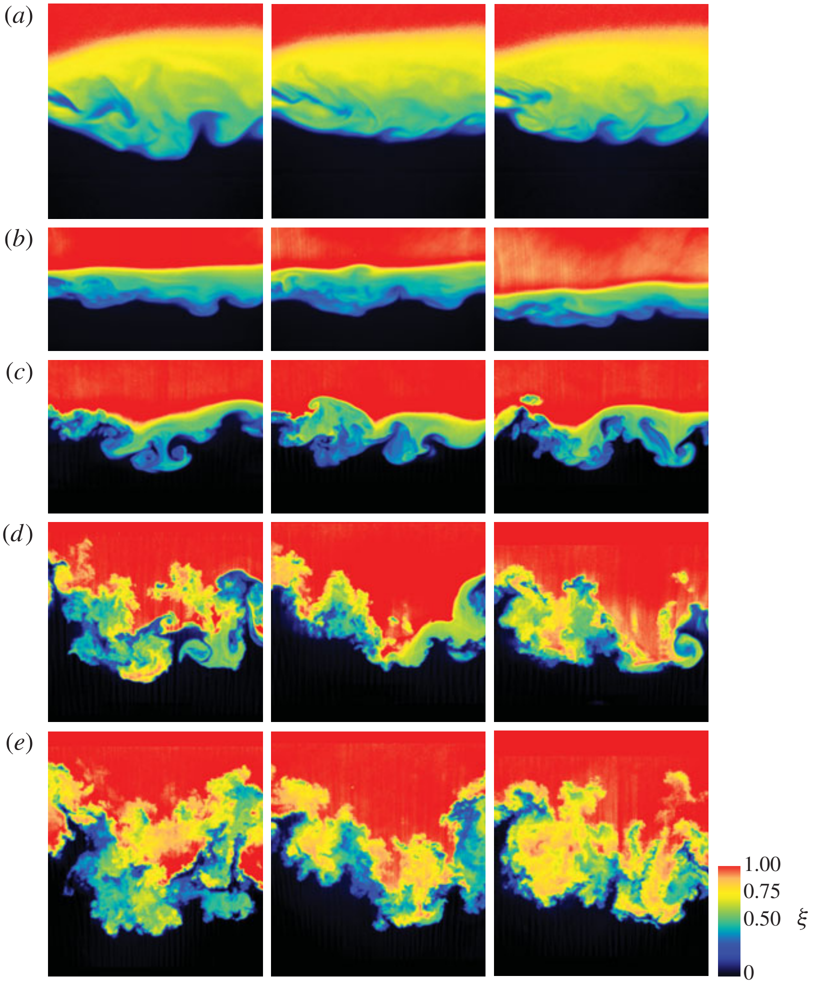

FIGURE 4. (Colour online) Selected images from $M = 2.2$ experimental sequence. First row: initial condition images. Second row: PS1, 0.10 ms after shock interaction. Third row: PS2, 0.44 ms after shock interaction. Fourth row: PS3, 1.12 ms after shock interaction. Fifth row: PS4, 2.05 ms after shock interaction. The width of each image is 14.0 cm.

compression from the shock wave. At the PS2 time, the layer is dominated by several spikes of heavy gas (coloured black) penetrating into the mixed gas (coloured blue and green). Coherent vortices are noticeable at this time and the interface contours appear relatively smooth. Some chaotic behaviour (jagged contours and more mixing) occurs on the left side of the layer. The slight left–right asymmetry is due to the flow in the initial condition, where the gases are injected on the left side, leading to sharper gradients on the left than on the right. Therefore, in some images the left side appears to transition to turbulence faster than the right. By the PS3 time, the smoothness that appeared along the interface is gone and many small-scale features are present. This trend continues into the PS4 time, where the mixing layer appears to be in a fully turbulent state (i.e. increased mixing and containing a broad range of scales). Isolated regions in the PS3 images can be noticed where the layer remains relatively smooth; these no longer exist by the PS4 time, where the full layer appears engulfed by turbulence.

The similarities between the two Mach number images are remarkable given the ∼2× difference in interface velocity. The post-shock image number (i.e. PS1, PS2, etc.) denotes the shock tube window used for the image and, between the two Mach numbers, represents the same post-shock travel distance ($V_o t$). Thus, the post-shock travel distance appears to qualitatively capture the turbulent evolution of the mixing layer. A few differences are apparent between the two Mach numbers. The greater compression of the $M=2.2$ flow results in a thinner mixing layer at the same window location. The composition of the layer also appears different at the last two times, where there appears to be more $\xi=0.75$ fluid (yellow colours) in the $M=2.2$ images.

3.2. *Mixing-layer thickness*

The thickness of the mixing layer, h_{5-95}, is defined as the distance between spanwise-averaged mole-fraction values of $\langle\xi\rangle=0.05$ and 0.95, where spanwise averaging, $\langle\cdot\rangle$, is

$$\langle\xi\rangle=\frac{1}{x_2-x_1}\int_{x_1}^{x_2}\xi\,\mathrm{d}x. \tag{3.1}$$

For the analysis that follows (except for the spectral analysis) the images are cropped to include only the central 8 cm, avoiding differences in the flow caused by the inlet. The mixing-layer thickness is shown in dimensional form in figure 5(*a*) from all of the experimental data. Since these images show a two-dimensional slice from a three-dimensional layer, a large amount of experimental variation is expected, and the average from the experiments, shown as open circles, is of the most relevance. A weighted, least-squares regression is used to calculate the initial linear growth rate at the earlier times. The inverse of the number of images at that post-shock time is used as the weighting in the regression, ensuring that the different times contribute equally despite having different numbers of images. The growth rates from the PS1–PS2 data are $\dot{h}_{5-95}=24.2\pm1.6\ \mathrm{m\ s^{-1}}$ and $35.4\pm7.3\ \mathrm{m\ s^{-1}}$ for $M=1.6$ and $M=2.2$, respectively. The ± value is the standard error in that measurement. Between the PS2 and PS3 times, the layer is growing at $\dot{h}_{5-95}=20.0\pm2.1\ \mathrm{m\ s^{-1}}$ and $27.0\pm4.1\ \mathrm{m\ s^{-1}}$ for $M=1.6$ and $M=2.2$, respectively, showing that the layer growth has slowed within this time frame.

The non-dimensional mixing-layer thickness is shown in figure 5(*b*). The thickness after shock compression, h_0', and the initial growth rate of the mixing layer, $\dot{h}_0$, provide excellent collapse of the two Mach number data. Also shown is the line

$$\frac{h}{h_0'}=\frac{\dot{h}_0}{h_0'}t+1 \tag{3.2}$$

and the power law

$$\frac{h}{h_0'}=a\left(\frac{\dot{h}_0}{h_0'}t\right)^{\theta}. \tag{3.3}$$

The power law fits the last three post-shock times with values of $a=1.98\pm0.01$ and $\theta=0.43\pm0.01$. This value of θ is in the upper range of previously reported values ($0.25\leqslant\theta\leqslant0.5$) in Dimonte & Schneider (1997, 2000), Prasad *et al.* (2000) and Jacobs *et al.* (2013).

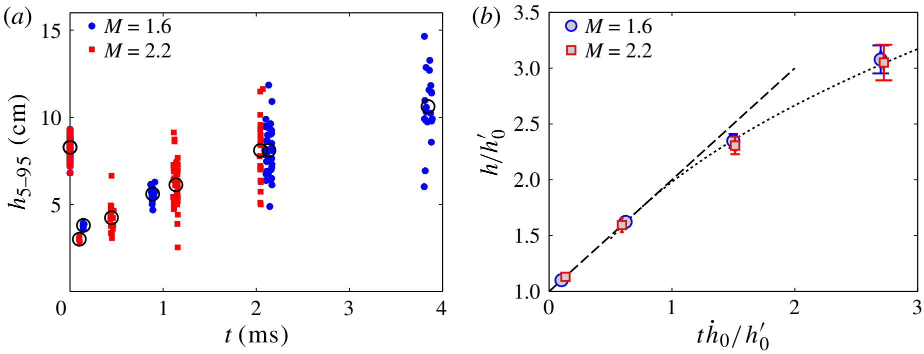

FIGURE 5. (Colour online) Mixing-layer thickness, h_{5-95}: (*a*) dimensional and (*b*) non-dimensional. Error bars in (*b*) show the standard error of the mean. Curve fits in (*b*) show a linear fit (dashed) and a power-law fit (dotted).

Both h'_0 and $\dot{h}_0$ were obtained from the linear fit to the PS1 and PS2 data, but these values can be estimated *a priori* if their dependence on the initial conditions is known. To understand the initial condition dependence for this interface, the initial growth rates of the two Mach numbers are compared with the initial condition dependence of two contrasting regimes: the linear growth of mixing layers following reshock and the linear growth of well-defined interfacial perturbations. In reshock experiments such as those of Vetter & Sturtevant (1995) and Leinov *et al.* (2009), the interface is characterized by a thickness that contains, presumably, a broad distribution of perturbations interspersed within the layer in a self-similar manner. These layers grow linearly after reshock at a rate that is independent of the pre-reshock thickness, $\dot{h} = C_M A' V_0$, which was proposed by Mikaelian (1989) and fits a number of experiments (Read 1984; Youngs 1984; Vetter & Sturtevant 1995; Leinov *et al.* 2009; Jacobs *et al.* 2013) with $C_M \approx 0.25$–0.49. If the perturbations on the interface between two gases are well-defined, then the initial growth rate is also proportional to the amplitude of the perturbations after shock compression, $\dot{h} = A' V_0 \eta' k$, where η' is the compressed amplitude of wavenumber k. A multimode interface would contain a superposition of growing modes. If the perturbations are nonlinear in amplitude, the relationship between growth rate and initial amplitude remains but is no longer directly proportional.

The interface used here lies between the two extremes of reshock-type initial conditions and well-defined interfacial perturbations. It contains identifiable perturbations, but they are not well-defined, as contour locations are multivalued in the spanwise direction and have different spectral content at different locations within the layer (see figure 2*d*). The perturbations are interspersed within the layer, but not self-similarly and only occupy $\sim 1/4$ of the full h_{5-95} thickness. The ratio of initial growth rates between the two Mach numbers, $\dot{h}_{M=2.2}/\dot{h}_{M=1.6}$, is compared with that expected by these two initial condition extremes. The experiments produce $\dot{h}_{M=2.2}/\dot{h}_{M=1.6} = 1.46 \pm 0.32$. If the growth rate were independent of initial conditions, a ratio of $(A'V_0)_{M=2.2}/(A'V_0)_{M=1.6} = 1.72$ would be expected. Alternatively, if the growth rate were also proportional to the compressed interface thickness the ratio would be 1.17. Here the compression factor was based on the pre- to post-shock density ratios, $h'_0/h_0 \approx (\rho_1/\rho'_1 + \rho_2/\rho'_2)/2$, which is within 10 % of the measured values. An alternative compression factor, introduced by Richtmyer (1960) and commonly used to estimate perturbation compression, is $(1 - V_0/W_i)$, where W_i is the incident shock wave speed and V_0 is the post-shock interface velocity (both of these compression factors are reported in table 1). Using this, a growth-rate ratio of 1.46 is expected, which is equal to the experimentally measured ratio. This suggests that the interface perturbations still factor into the measured initial growth rate.

3.3. *Mixing-layer composition*

The composition of the mixing layer is explored through PDFs of mole fraction. These two-dimensional PDFs, shown in figure 6, are given as a function of non-dimensional z-location, $\tilde{z} = z/h_{5-95}$, and are ensemble-averaged from the data set. Darker colours represent an increased probability of mole fraction at a given location. Note that integrating this PDF at a given $\tilde{z}$ location will give the spanwise-averaged mean,

$$\langle \xi \rangle \, (\tilde{z}) = \int \mathrm{PDF}\,(\xi, \tilde{z})\, \xi \, \mathrm{d}\xi, \tag{3.4}$$

and the standard deviation,

$$\sigma\,(\tilde{z}) = \sqrt{\int \mathrm{PDF}\,(\xi, \tilde{z})\, (\xi - \langle \xi \rangle)^2 \, \mathrm{d}\xi}. \tag{3.5}$$

By definition $\langle \xi \rangle = 0.05$ or 0.95 at $\tilde{z} = z/h_{5-95} = -0.5$ or 0.5, respectively. At the location near $\tilde{z} \approx 1$ there is expected to only be $\xi = 1.0$ fluid, therefore the spread in the PDF (i.e. the standard deviation) is due to measurement errors (shot noise and uncorrected features in the laser sheet). Thus, the standard deviation in this region ($\sigma = 0.03$ for the IC and 0.04 for the post-shock images) gives the error in the mole fraction measurement. These values agree with the expected error given the signal-to-noise ratio of 30 for the raw images.

The first row of figure 6 shows that the initial condition mole fraction gradually transitions from $\xi = 1$ at the top of the mixing layer to $\xi \sim 0.4$ near the bottom. This gradual marching behaviour is due to the diffusive spreading of the inlet jet, which, as seen in figure 2, does not contain large-scale inhomogeneities (Kelvin–Helmholtz features) aside from the very bottom of the layer. The perturbations at the bottom of the mixing layer show up as a wide region in the PDF, containing mole fractions between $\xi = 0$ and $\xi = 0.4$.

The second post-shock realization (second row) shows a PDF that has spread out over a wider extent of mole fractions; nearly all of the mixing layer contains a finite probability between $\xi = 0$ and $\xi = 0.6$. The transition between $\xi = 0.6$ and $\xi = 1$ is still confined to the top of the mixing layer as the growing perturbations that began on the bottom of the layer have not significantly influenced this region yet.

By the PS3 time, the perturbations have reached the top of the layer, entraining high mole fraction gas and distributing it throughout the mixing layer. This is evident by the $\xi = 0.6$ to $\xi = 1$ mole fraction now having a larger probability throughout most of the mixing layer. By this time, the peak in the PDF of mixed fluid ($\xi \sim 0.4$) is significantly reduced in the $M = 2.2$ experiments.

At the latest time, the transition from $\xi = 0$ to $\xi = 1$ is more gradual than earlier times, particularly in the $M = 2.2$ experiments. The peak near $\xi \sim 0.4$ still exists at the lower Mach number but is almost completely removed through mixing in the higher Mach number experiments.

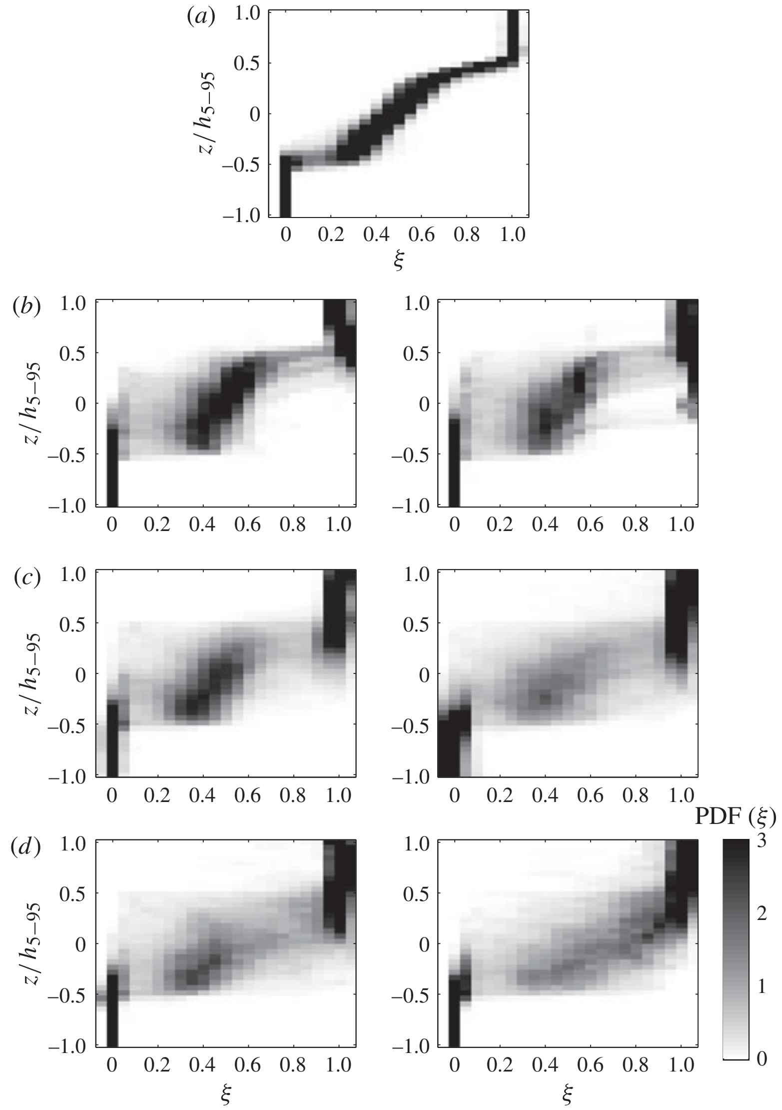

FIGURE 6. PDF of mole fraction throughout the mixing layer for the (*a*) IC, and (*b*,*c*) PS2, (*d*,*e*) PS3 and (*f*,*g*) PS4 from the (*b*,*d*,*f*) $M = 1.6$ experiments and (*c*,*e*,*g*) $M = 2.2$ experiments. The z-axis is normalized by the $\langle \xi \rangle = 0.05$–$0.95$ thickness, h_{5-95}.

The overall composition of the mixing layer (within $0.05 < \langle \xi \rangle < 0.95$) is obtained from the 2D PDFs by

$$\mathrm{PDF}\,(\xi) = \int_{-0.5}^{0.5} \mathrm{PDF}(\xi, \tilde{z})\,\mathrm{d}\tilde{z}, \tag{3.6}$$

and is shown in figure 7 for the (*a*) $M = 1.6$ data and (*b*) $M = 2.2$ data. The PDFs show that local peak near $\xi \sim 0.4$ reduces over time and appears to mix with the lighter ($\xi = 1$) fluid. This process occurs more rapidly in the $M = 2.2$ case and results in an increase in the fluid near $\xi \sim 0.8$. This bias for mixing of the lighter fluids

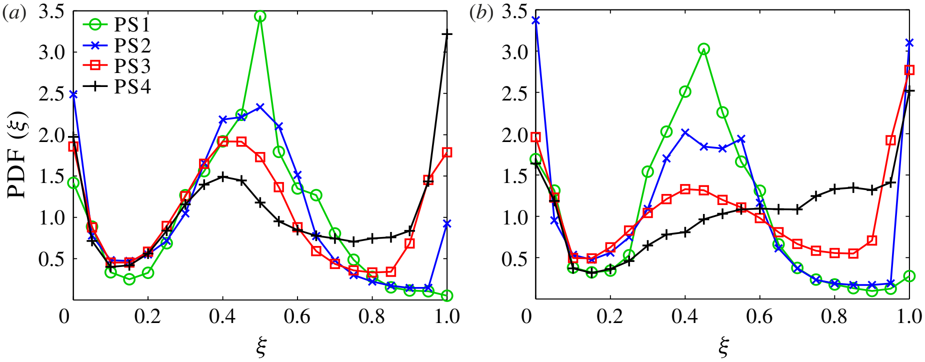

FIGURE 7. (Colour online) PDF of mole fraction within $0.05 < \langle\xi\rangle < 0.95$: (*a*) $M = 1.6$ and (*b*) $M = 2.2$.

has been noticed elsewhere and is attributed to the greater inertia of the heavy fluid (Livescu & Ristorcelli 2008).

A metric describing the state of mixing can be constructed from the ratio of the ‘thickness of mixed fluid’ to the mixing layer thickness. Mixed fluid is defined following Cook & Dimotakis (2001) as limited by the lesser component in a stoichiometric mixture,

$$\xi_m(\xi) = 2\ \min(\xi, 1 - \xi), \tag{3.7}$$

thus an equal mixture would have $\xi_m = 1$. With this definition, the mixing layer thickness is

$$h_m = \int_{-\infty}^{\infty} \xi_m(\langle\xi\rangle)\,\mathrm{d}z, \tag{3.8}$$

and is shown in figure 8(*a*) to be proportional to h_{5-95} ($h_m = 0.57h_{5-95}$). These definitions of mixing-layer thickness do not differentiate between mixed gas and unmixed but interpenetrating gas. These are compared in the following ratio:

$$\varXi = \frac{\displaystyle\int_{-\infty}^{\infty} \langle\xi_m(\xi)\rangle\ \mathrm{d}z}{\displaystyle\int_{-\infty}^{\infty} \xi_m(\langle\xi\rangle)\ \mathrm{d}z}, \tag{3.9}$$

where the denominator is the same as (3.8) and the numerator averages after converting the mole fraction field into a mixture fraction field. A fully homogenized fluid without interpenetrating perturbations will have a ratio of $\varXi = 1$, while a discontinuous interface with perturbations would have $\varXi = 0$. In these experiments, this ratio, shown in figure 8(*b*), begins near $\varXi = 1$ for both IC and PS1, signifying that the thickness of the layer mostly comes from mixed fluid and not from perturbations. In the $M = 1.6$ case, $\varXi$ reduces steadily throughout the experiment, while $\varXi$ in the $M = 2.2$ case reduces more rapidly (in non-dimensional time) before increasing at the end. Both Mach numbers reach a final value of 0.79, which is close to the asymptotic value of 0.8 reported after the onset of turbulent mixing in Rayleigh–Taylor simulations (Cook, Cabot & Miller 2004). This final value is slightly lower than the asymptotic values of 0.82–0.93 in gas-curtain experiments (Orlicz, Balasubramanian & Prestridge 2013), which observed $\varXi$ to increase with Mach number. The different temporal behaviour seen in figure 8(*b*) between these

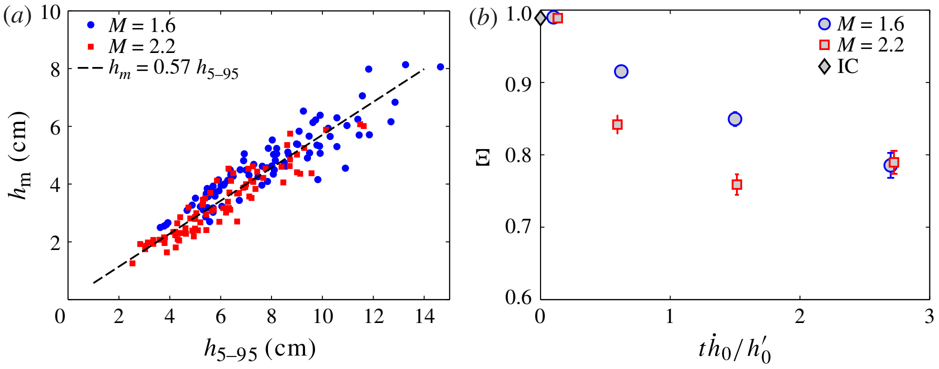

FIGURE 8. (Colour online) (*a*) Comparison of mixing layer thickness definitions, h_m versus $h_{5\text{–}95}$. (*b*) Ratio of the mixed fluid thickness to the mixing layer thickness, Ξ.

two cases may represent differences in the balance of modal growth and molecular mixing. In the higher-Mach-number case, modal growth may be dominating earlier in the experiment, bringing in unmixed fluid and more-rapidly decreasing Ξ. A transition may occur near PS3 of the $M = 2.2$ case, causing molecular mixing to dominate towards the end. The less-rapid rate of change of Ξ at the lower Mach number may imply that these two forces are more balanced.

3.4. *Density self-correlation*

An additional measure of fluid mixing and an important quantity for turbulence modelling is the density self-correlation,

$$b = -\left\langle \rho^* \left(\frac{1}{\rho}\right)^* \right\rangle, \tag{3.10}$$

where asterisks denote spanwise variations, i.e. $\rho^* = \rho - \langle\rho\rangle$. In the variable-density Reynolds-averaged equations, b appears in the production term for the mass flux and requires modelling for closure (Besnard *et al.* 1992). One approach for closure is to make a Boussinesq approximation (Grégoire, Souffland & Gauthier 2005), in which case b reduces to

$$b_{Boussinesq} = \frac{\langle \rho^{*2} \rangle}{\langle\rho\rangle^2}. \tag{3.11}$$

This approximation has been found to be adequate at modest Atwood numbers (Livescu *et al.* 2009; Ristorcelli, Gowardhan & Grinstein 2013).

Here the density field is approximated as

$$\rho = \rho'_2 + (\rho'_1 - \rho'_2)\xi. \tag{3.12}$$

Figure 9 shows the spanwise-averaged mole fraction profile across the layer, $\langle\xi\rangle$ (left axis), b (right axis, solid) and $\langle\rho^{*2}\rangle/\langle\rho\rangle^2$ (right axis, dashed) for (*a*) $M = 1.6$ and (*b*) $M = 2.2$. Shock compression reduces $\langle\xi\rangle$ in the interior of the layer (i.e. at $z/h_{5\text{–}95} = 0$), partially due to differences in the compressibilities of the heavy and light gases. By the PS3 and PS4 times, $\langle\xi\rangle$ has increased in the interior of the layer, but does not yet show a self-similar profile. The density self-correlation at the first post-shock time is similar to its value in the initial condition and both are much

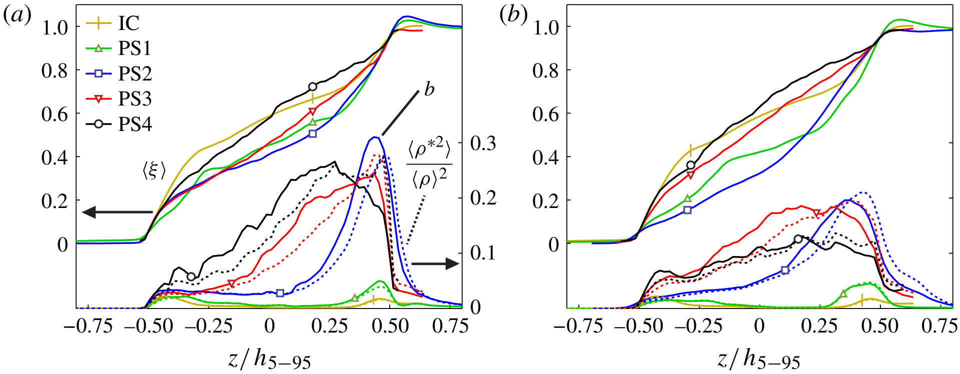

FIGURE 9. (Colour online) Density self-correlation, b (right axis, solid), normalized density variance, $\langle\rho^{*2}\rangle/\langle\rho\rangle^2$ (right axis, dashed), and mean mole fraction, $\langle\xi\rangle$ (left axis): (*a*) $M = 1.6$ and (*b*) $M = 2.2$.

smaller than at later times. At PS2 a large peak in the b profile appears near the lower density edge of the layer. By the latest two times the peak is centred closer to the centre of the layer but the profile is still shifted towards the lower density side. In the $M = 1.6$ case, b is still increasing through most of the layer between the latest two times, but in the $M = 2.2$ case b is decreasing by the latest time, suggesting it is in a more well-mixed state. Aside from the late-time differences, the trends for the two Mach numbers are similar, but the values for the lower Mach number case are $\sim$50 % larger.

The values of b measured here are a factor of 2–3 times larger than those measured in the gas-curtain RMI experiments (Balakumar *et al.* 2012) and in gas-channel RTI experiments (Banerjee, Kraft & Andrews 2010). This is likely due to the presence of unmixed spikes in these experiments that protrude through the mixing layer even at late times. Despite the large range of densities, the Boussinesq approximation, $\langle\rho^{*2}\rangle/\langle\rho\rangle^2$, closely tracks the trend observed in b. As noted by Livescu *et al.* (2009) for RTI simulations, $\langle\rho^{*2}\rangle/\langle\rho\rangle^2$ tends to over-predict b on the low-density side of the layer and under-predict it on the high-density side.

3.5. *Scalar variance spectra*

The scale distribution of the mole fraction fields is reported here using one-dimensional scalar variance energy spectra. The spectra are computed horizontally within the region $0.1 < \langle\xi\rangle < 0.7$ and includes the full width of the laser sheet (15.5–19.5 cm). For $\langle\xi\rangle > 0.7$, the IC-PS2 spectra deviated from the relatively similar spectral shape observed in the $0.1 < \langle\xi\rangle < 0.7$ region, so only this lower region was used to produce average spectra. Using only the central 8 cm of the images' width produced nearly identical spectra, but the full width allowed for lower wavenumbers to be resolved. To reduce the influence of noise, an interlacing technique is used (Kaiser & Frank 2007) where the Fourier coefficient, $F(\xi(x))$, is multiplied by the complex conjugate of the Fourier coefficient of the adjacent row,

$$E(k_x) \approx F(\xi_j(x))F^*(\xi_{j+1}(x)). \tag{3.13}$$

Since photonic shot noise is uncorrelated from pixel to pixel, and assuming neighbouring rows record a similar turbulence structure, the noise contribution tends

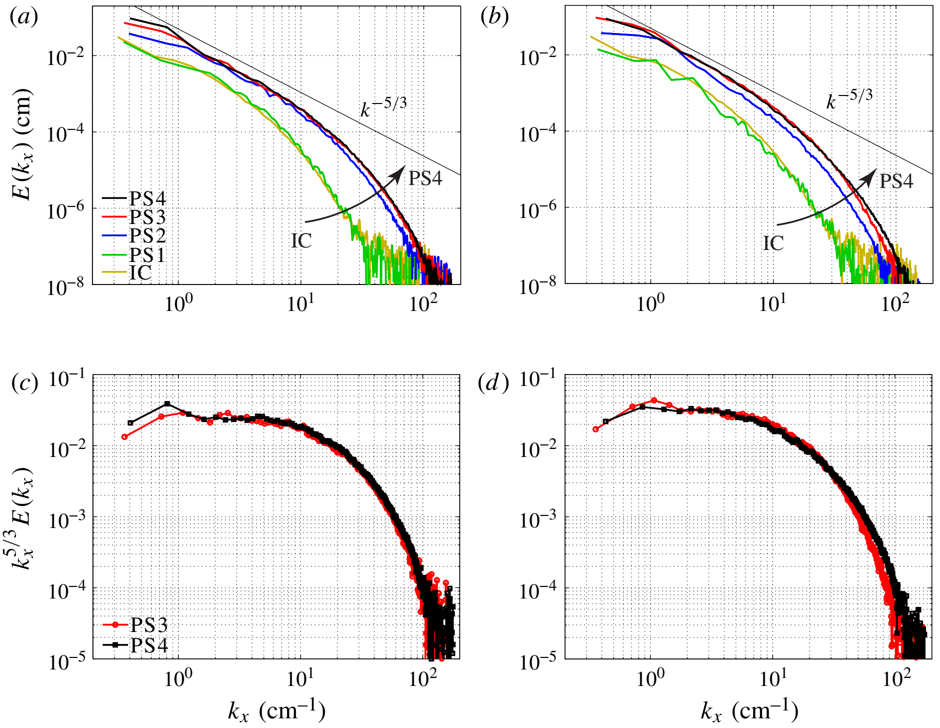

FIGURE 10. (Colour online) One-dimensional scalar variance energy spectra, (*a*) $M = 1.6$ and (*b*) $M = 2.2$, and compensated spectra, (*c*) $M = 1.6$ and (*d*) $M = 2.2$.

towards zero with an average of these interlaced spectra. The spectra were found to be converged with 10–20 images. The spectra are normalized to integrate to the scalar variance, i.e.

$$\int E \mathrm{d}k_x = \left\langle \xi^2 \right\rangle - \langle \xi \rangle^2 . \tag{3.14}$$

Figure 10 shows the spanwise 1D energy spectra for the five times from the (*a*) $M = 1.6$ and (*b*) $M = 2.2$ data. The spectra from the IC and PS1 lie very close to each other, as would be expected given the very early time of PS1. Between PS1 and PS2 the magnitude of the spectrum increases, representing an increase in scalar variance. The spectra of the last three times, PS2–PS4, are very similar, which is interesting given the visual difference between the corresponding images in figures 3 and 4. The magnitude of the high-wavenumber region is increasing through the latest time. An apparent $k^{-5/3}$ inertial range is noticeable at the latest three times. This inertial range manifests for approximately a decade in wavenumbers before an exponential dissipation region is observed. The compensated spectra are shown in figure 10(*c*,*d*) for the $M = 1.6$ and $M = 2.2$ data, respectively and show a region between 0.7 and 7 cm^{-1} that is nearly flat, although a slight negative slope appears present. A least-squares fit to the $1\ \mathrm{cm}^{-1} < k < 5\ \mathrm{cm}^{-1}$ region finds $E \propto k^{-1.72}$ and $E \propto k^{-1.76}$ at PS4 for the $M = 1.6$ and $M = 2.2$ cases, respectively.

3.6. *Turbulent length scales*

In this section, turbulent length scales are measured from within the mixing layer using the mole fraction fields. Of primary interest are the Taylor microscale and the viscous scale, as their relationship governs turbulent mixing. From these length scales, a Reynolds number is computed and the turbulent transition is discussed.

3.6.1. *Batchelor scale*

The inner viscous scale separates the inertial range from the dissipation range, but this can be difficult to identify in an experimental spectrum. Instead, the spectrum can be compared with a model velocity spectrum, where the relevant length scales are known (Wang *et al.* 2007; Petersen & Ghandhi 2011). Pope (2000) proposed the following model for 3D isotropic, homogeneous turbulence:

$$E_{3D}(k) = C_p \left\langle \varepsilon \right\rangle^{2/3} k^{-5/3} f_L(kL) f_\eta \left(k\eta_k\right), \tag{3.15}$$

with a dissipation region

$$f_\eta \left(k\eta_k\right) = \exp\left(-\beta\left(\left[(k\eta_k)^4 + c_\eta^4\right]^{1/4} - c_\eta\right)\right), \tag{3.16}$$

where η_k is the Kolmogorov length scale and β and c_η are chosen to fit experimental data. Pope found an excellent fit to a range of homogeneous, isotropic experimental data with $C_p = 1.5$, $\beta = 5.2$ and $c_\eta = 0.4$. Alternatively, the dissipation region is a simple exponential when $c_\eta = 0$, and β is constrained to $\beta = 2.1$ by requiring (3.15) to integrate to the net turbulent kinetic energy and dissipation. The low-wavenumber specification to the model spectrum, $f_L(kL)$, gives the spectrum an $E_{3D} \sim k^2$ shape. Since the spectra from the present data do not clearly depart from a power law on the low-wavenumber side, the $f_L(kL)$ function is not included, allowing the model spectrum to continue as $k^{-5/3}$ into the low wavenumbers. The one-dimensional energy spectrum is obtained through integration of the three-dimensional spectrum (Tennekes & Lumley 1972),

$$E(k_1) = \int_{k_1}^{\infty} k^{-1} E_{3D}(k)\, \mathrm{d}k. \tag{3.17}$$

The dissipation spectrum is related to the energy spectrum by $D(k) = 2\nu k^2 E(k)$, where ν is the kinematic viscosity. Using Pope's model spectrum, one finds that the dissipation spectrum reaches 2 % of its peak at $k\eta_k = 1$. Therefore, measuring the 2 % dissipation level allows one to infer the Kolmogorov scale. This requires a resolution of $\pi\eta_k$. In passive scalar turbulence, the smallest length scale is the Batchelor scale, λ_B, which is related to the Kolmogorov length scale by the Schmidt number ($Sc = \nu/\mathscr{D}$), $\lambda_B = \eta_k Sc^{-1/2}$, where $Sc \approx 1$ for gases.

The dissipation spectra from the PS4 data are shown in figure 11 and the 2 % dissipation level is indicated. The $1/k_{2\%}$ scale occurs at a wavelength of $2\pi/k_{2\%}$, requiring a resolution of $\pi/k_{2\%}$ or ~350 μm, which is ~2 × the camera resolution (pixel size) or half of the Nyquist frequency. The imaging system's modulation transfer function (MTF) is approximately 0.4 at this scale, thus this scale is expected to be overestimated by the resolution limits. Photonic shot noise, however, would cause this measurement to be underestimated. This noise effect is thought to be removed by the interlacing technique, but there remains uncertainty in its efficacy. Another way of estimating the Batchelor scale, and avoiding some of the uncertainty at the highest wavenumbers, is to fit Pope's model to the experimental spectrum using λ_B as a fitting parameter. A least-squares fitting procedure is biased towards finding the dissipation spectra peak, where the MTF is still at 1.0. Pope's model, also shown in figure 11, appears to fall off more sharply than the experimental data and values of λ_B are found

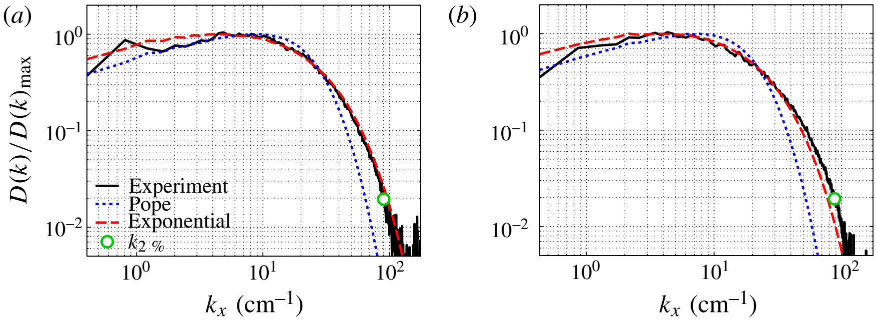

FIGURE 11. (Colour online) Dissipation spectrum from the latest post-shock time and model spectra: (*a*) $M = 1.6$ and (*b*) $M = 2.2$.

to be approximately 50 % larger than the measured $1/k_{2\,\%}$ scale. These two methods give a range of estimates for the Batchelor scale. The value from fitting Pope's model is likely an upper bound, while the smaller $1/k_{2\,\%}$ scale is not necessarily the lower bound. It is interesting to note that a better fit to the high wavenumber region is found using the exponential version of Pope's model (i.e. $c_\eta = 0$ in (3.16)).

An additional length scale based on the Batchelor scale, the dissipation layer thickness, is computed as a comparison with the length scales computed from the dissipation spectra. The scalar dissipation rate field, $\chi = \mathscr{D}\nabla\xi \cdot \nabla\xi$, is observed consisting of sheet-like structures (Buch & Dahm 1996, 1998; Tomkins *et al.* 2008; Orlicz *et al.* 2009). These structures arise from the compressive action of the strain rate, which stretches contour lines and increases the scalar gradients, and the thickening action of diffusion. Thus an equilibrium exists where these forces balance, resulting in a scalar dissipation length scale (Su & Clemens 2003),

$$\lambda_{20\,\%} = \Lambda\lambda_B. \tag{3.18}$$

The proportionality constant Λ has been found to range from 2 to 14.9 (Buch & Dahm 1998; Su & Clemens 2003; Wang *et al.* 2007) and may be flow-dependent. The '20 %' in (3.18) refers to a method to measure this scale: the thickness where the dissipation rate drops to 20 % of its local peak.

To compute the dissipation rate field, the mole fraction images are filtered through a 5 × 5 median filter, chosen to reduce shot noise and preserve spatial resolution (Ghandhi 2006), and the gradient magnitude is calculated using an 8-point stencil (Buch & Dahm 1996). For simplicity, the molecular diffusivity, $\mathscr{D}$, is treated as constant, therefore its magnitude does not influence the measurement of $\lambda_{20\,\%}$. To identify peaks in the dissipation rate field, a Canny edge detection algorithm (Canny 1986) is applied to the image of dissipation rate, which finds the local maxima of the gradients. From these peaks, the dissipation rate in directions aligned with the local gradient angle is computed through interpolation. The distance where the dissipation rate drops to 20 % of the local maximum is recorded as half the $\lambda_{20\,\%}$ value. Points are discarded if (i) the local dissipation rate maximum is less than a given threshold, (ii) the dissipation rate does not decrease to 20 % monotonically, (iii) the dissipation rate does not decrease to 20 % within a certain distance or (iv) if a value for $\lambda_{20\,\%}$ is not found on both sides of a local maximum. An example of this calculation is shown in figure 12, where the inset shows the dissipation rate and the detected $\lambda_{20\,\%}$ lengths.

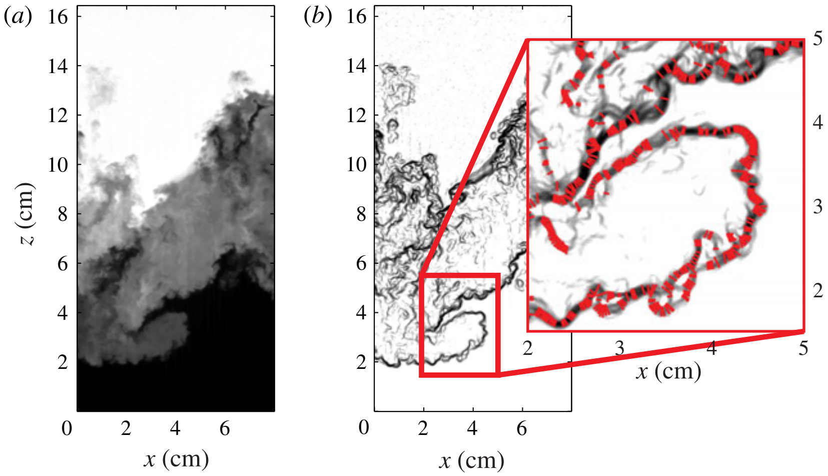

FIGURE 12. (Colour online) Dissipation layer thickness measurement example. Left images shows mole fraction from a $M = 1.6$ PS4 image. Middle image shows the dissipation rate. Zoomed-in image shows the 20 % thickness of detected dissipation structures.

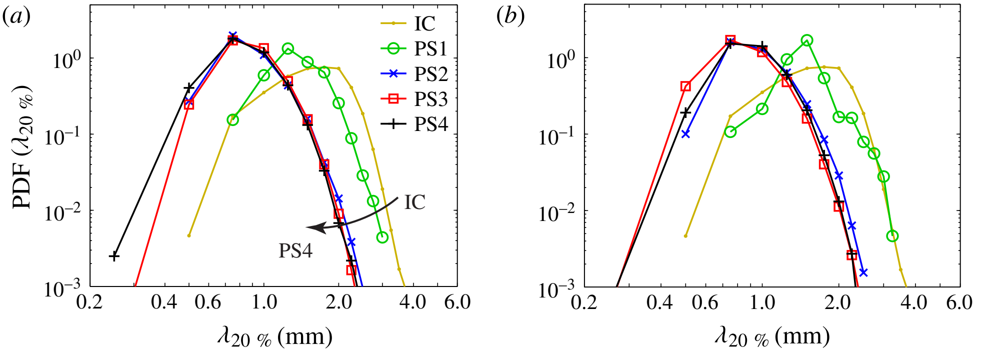

FIGURE 13. (Colour online) PDFs of dissipation layer thickness: (a) $M = 1.6$ and (b) $M = 2.2$.

The PDF of the dissipation layer thickness is shown in figure 13 for the different times and Mach numbers. There is a noticeable trend of decreasing scales up until the last three post-shock times, where the PDFs all collapse to a similar curve. The peak in the late-time PDFs is at 0.75 mm, which is $\sim 5\times$ the standard deviation of the line spread function. From this resolution there is an estimated 25 % error in the dissipation length scale measurements at the late post-shock times (Wang & Clemens 2004). The trend of decreasing $\lambda_{20\,\%}$ is notable despite the resolution limits. This scale is compared with the Batchelor scale from the dissipation spectra in figure 14. A proportionality constant of $\Lambda \approx 5$ scales $\lambda_{20\,\%}$ to λ_B at the last three post-shock times. This is within the range of previously reported values for Λ (Buch & Dahm 1998; Su & Clemens 2003; Wang *et al.* 2007). All of the measurements in figure 14 show a trend of decreasing scale for the first three times (IC, PS1, and PS2). The flattening out at the last three times may be a consequence of resolution limitations.

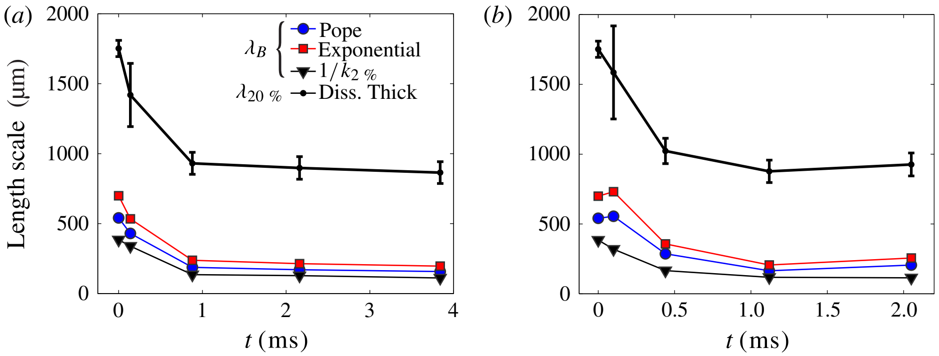

FIGURE 14. (Colour online) Batchelor and dissipation length scales: (*a*) $M = 1.6$ and (*b*) $M = 2.2$.

3.6.2. *Taylor microscale*

The Taylor microscale is defined based on the curvature of the scalar or velocity autocorrelation. The scalar variance autocorrelation,

$$R(r) = \frac{\langle \xi^*(x)\xi^*(x+r)\rangle}{\langle (\xi^*)^2 \rangle}, \tag{3.19}$$

is symmetric, $R(-r) = R(r)$, so the first terms in the Taylor series are

$$R(r) = 1 + \frac{1}{2}\frac{\mathrm{d}^2 R(0)}{\mathrm{d}r^2} r^2 \tag{3.20}$$

$$= 1 - \frac{r^2}{\lambda_T^2}, \tag{3.21}$$

where λ_T is the Taylor microscale. This scale can be calculated directly from the curvature of the autocorrelation (Champagne, Harris & Corrsin 1970; Ramaprabhu & Andrews 2004; Petersen & Ghandhi 2011),

$$\lambda_T = \left[-\frac{1}{2}\frac{\mathrm{d}^2 R(0)}{\mathrm{d}r^2} \right]^{-1/2}, \tag{3.22}$$

or, equivalently, it can be calculated from the variance and the first derivative,

$$\lambda_{T,x} = \left[\frac{2\left\langle (\xi^*)^2 \right\rangle}{\left\langle \left(\dfrac{\partial \xi^*}{\partial x} \right)^2 \right\rangle} \right]^{1/2}, \quad \lambda_{T,z} = \left[\frac{2\left\langle (\xi^*)^2 \right\rangle}{\left\langle \left(\dfrac{\partial \xi^*}{\partial z} \right)^2 \right\rangle} \right]^{1/2}. \tag{3.23a,b}$$

Both methods are explored here.

When calculating $\langle \xi^*(x)\xi^*(x+r)\rangle$ within the domain $[x_1, x_2]$, the spanwise averaging operator needs modification to avoid zero-biasing and ensure symmetry. Therefore, for the autocorrelation, the following is used

$$\langle \xi^*(x)\xi^*(x+r)\rangle = \frac{1}{x_2 - x_1 - r}\int_{x_1}^{x_2 - r} \xi^*(x)\xi^*(x+r)\,\mathrm{d}x. \tag{3.24}$$

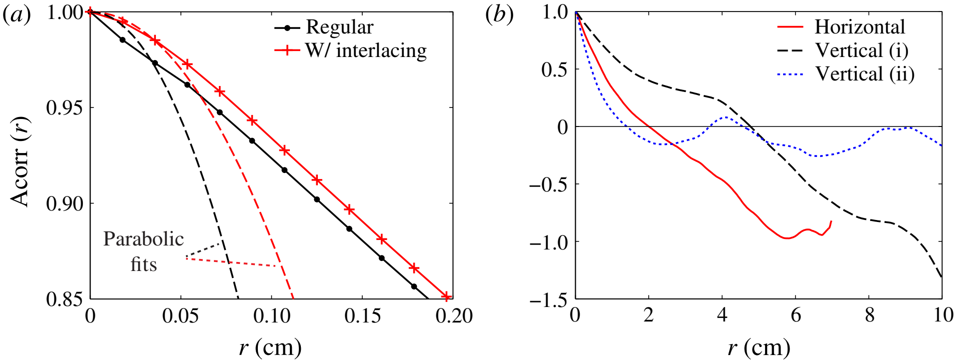

FIGURE 15. (Colour online) Autocorrelation examples: (*a*) horizontal, zoomed in to show interlacing technique and (*b*) the full autocorrelation in the horizontal and vertical directions (using the two subtraction methods).

From the cross-correlation theorem, the transform of the autocorrelation is equivalent to the square of the magnitude of the Fourier transform of the single variable, in this case ξ. The autocorrelation can then efficiently be computed through the inverse transform, with appropriate normalization. We take advantage of this and use the interlacing technique, equation (3.13), when computing the transform. This avoids some of the loss in correlation that occurs due to noise. The effect of this is small, as shown in figure 15(*a*), but it improves the calculation of the Taylor microscale, producing a curve that appears more parabolic near the $r = 0$ point. For this example, the parabola fits the interlaced autocorrelation curve with 2.6 % error in the Taylor microscale value, while 7.3 % error is found when fit to the regular autocorrelation curve. The full autocorrelation is shown in figure 15(*b*) in the horizontal and vertical directions. The horizontal autocorrelation, computed after subtracting the spanwise-averaged profile from the image, continues downward into the negative region due to the presence of low wavenumber structures in the layer. The vertical autocorrelation is computed in two ways: (i) subtracting the vertical average of each column before calculating the autocorrelation and (ii) subtracting both the spanwise average and the vertical average. These two methods are shown in figure 15(*b*). The vertical autocorrelation computed using the first method, subtracting the vertical average, becomes inversely (negatively) correlated over large distances. This is because the mole fraction goes from $\xi = 0$ in the bottom of the image to $\xi = 1$ in the top. This issue is mitigated by also subtracting the spanwise-averaged profile from the image, which causes the autocorrelation to oscillate near zero at larger distances and is similar to the horizontal curve at small distances.

The Taylor microscale is computed from the curvature of the autocorrelation curve at $r = 0$. The chosen method is to fit a parabola to the central seven points, i.e. the central $r = 0$ point, the next three points and the equivalent three points on the negative r side of the autocorrelation. Using different numbers of points or using a second-order central difference at $r = 0$ produces proportional results but appears to have more scatter over the different experiments. As shown below, this seven-point fitting method gives similar results to a different Taylor microscale calculation in the horizontal direction.

An alternate method for calculating the Taylor microscale, used in RTI simulations (Ristorcelli & Clark 2004; Cabot & Cook 2006), is through the variance and the

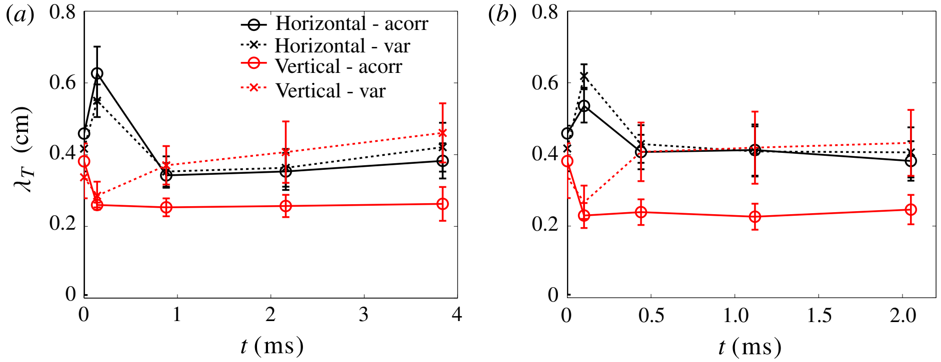

FIGURE 16. (Colour online) Taylor microscale: (*a*) $M = 1.6$ and (*b*) $M = 2.2$. Error bars show the standard error of the mean.

gradient (3.23). The averaging is performed in the spanwise direction for both the horizontal and vertical directions. The error in this measurement can be estimated from the work of Wang *et al.* (2007), where the degradation in the mean variance and scalar dissipation (i.e. the numerator and denominator of (3.23)) are computed based on resolution. With the smallest measured Batchelor scale from the previous section, the Taylor microscale would be overestimated by only 2 % based on the resolution ($\sigma_{LSF}/\lambda_B = 1.3$). If the Batchelor scale were actually 2× smaller than this value, the Taylor microscale would be overestimated by 15 %, 4 × would produces a 66 % overestimate. The Taylor microscale values are compared in figure 16, where 'acorr' refers to the parabolic fit to the autocorrelation and 'var' refers to the variance/gradient method (3.23). The two methods produce similar results in the horizontal direction, with a magnitude near 4 mm and little change in the last three post-shock times. In the vertical direction there is nearly a factor of two difference between the two methods for some of the post-shock times. Both methods start with a vertical Taylor microscale that is smaller than the horizontal scale. In the variance-based method, the scale appears to be slightly larger than the horizontal scale by the latest time, while the autocorrelation-based method produces a vertical scale that stays below the horizontal scale. The expected evolution of the layer supports the trend observed in the variance-based method. (i) The vertical scales should start smaller than the horizontal scales due to the shock compression of the layer. (ii) In time, simulations of RTI and RMI turbulence note a persistent anisotropy with larger vertical Taylor microscales (although based on the velocity, not on scalars) (Cabot & Cook 2006; Lombardini, Pullin & Meiron 2012). For these reasons, the variance-based method is used in the following discussion.

3.7. *Length scales and Reynolds number discussion*

The values of the Batchelor and Taylor scales measured above appear large compared with those computed through Reynolds number scaling. We estimate below a Reynolds number of 6×10^4 for the $M = 1.6$ experiments at late times. Using this, one could estimate the Batchelor scale as $\lambda_B = Re^{-3/4}h = 28$ μm, where the final average h_{5-95} thickness of 10.6 cm is used. Similarly, the Taylor microscale could be estimated as $\lambda_T = 2.3Re^{-1/2}h = 1.0$ mm. Both of these values are 4× smaller than measured. The resolution effects discussed in the previous section do not make up for this

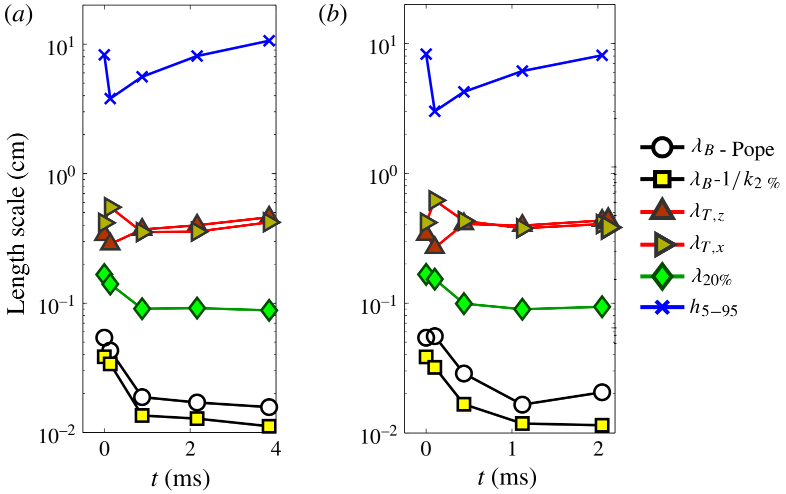

FIGURE 17. (Colour online) Summary of length scales: (a) $M = 1.6$ and (b) $M = 2.2$. The markers represent, from left to right, IC, PS1, PS2, PS3 and PS4.

discrepancy, as a 4× overestimate of λ_B would reduce the actual λ_T by only 1.66×. This may imply that the traditional Reynolds number scaling laws ((1.1) and (1.2)) may need modifications (different coefficients) when applied to RMI or variable density turbulence to produce length scales that agree with measurements. Using Reynolds number scaling in a similar flow, Tomkins *et al.* (2013) estimate a value of $\lambda_T = 0.14$ mm, thus it would be interesting whether (3.22) or (3.23) predict larger values in a similar manner.

Some of the length scales discussed previously are summarized in figure 17. A picture of scale separation emerges from this figure, with the largest scale, h_{5-95}, getting larger, the smallest scale, $\lambda_{20\,\%}$ and λ_B, getting smaller, and the intermediate scale, λ_T, staying approximately the same or slightly increasing.

The Reynolds number can be measured from the Batchelor and Taylor scales. From the ratio of their Reynolds number dependence ((1.1) and (1.2)),

$$\frac{\lambda_T}{\lambda_B} = \frac{2.3\mathcal{L}Re^{-1/2}}{\mathcal{L}Re^{-3/4}}, \tag{3.25}$$

the outer-scale Reynolds number is

$$Re \simeq \frac{1}{28}\left(\frac{\lambda_T}{\lambda_B}\right)^4. \tag{3.26}$$

By definition, $Re > 1 \times 10^4$ for this equation is equivalent to $\lambda_L/\lambda_\nu > 1$. The Reynolds number is computed and shown in figure 18. Curves are shown for each Mach number and separate calculations of (3.26) are made using the Batchelor scale from the $1/k_{2\,\%}$ value and from the fit to Pope's model spectrum. The horizontal Taylor microscale, calculated using (3.23), is used. Also shown in figure 18 is a definition for outer-scale Reynolds number commonly used in RMI and RTI computational studies,

$$Re = \frac{h\dot{h}}{\nu}. \tag{3.27}$$

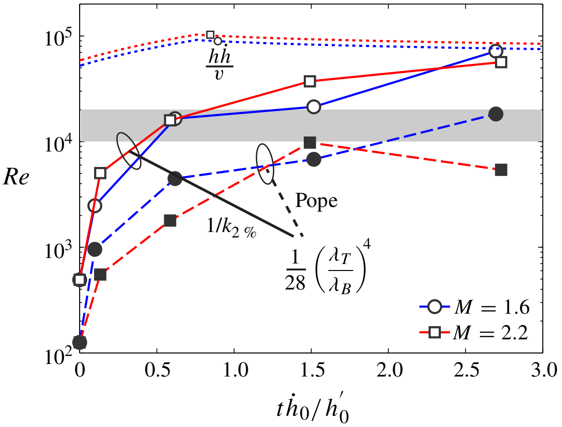

FIGURE 18. (Colour online) Reynolds number measurements. Here $M = 1.6$ in blue and $M = 2.2$ in red. Dotted lines use (3.27) and the curve fits of figure 5(*b*). Solid and dashed lines use (3.26), measuring λ_B using the $1/k_{2\,\%}$ method and fitting to Pope's model, respectively. The markers attached to the solid and dashed lines represent, from left to right, IC, PS1, PS2, PS3 and PS4. The grey band indicates the threshold for turbulent mixing (Dimotakis 2000).

Here this equation is evaluated using the linear and power-law curve fits from figure 5(*b*). The kinematic viscosity is computed as $\nu(\xi) = \mu_{mix}/(\rho'_2 + (\rho'_1 - \rho'_2)\xi)$ and the dynamic viscosity is averaged from the viscosities of each species, weighted by its mole fraction and molecular weight (Reid, Prausnitz & Poling 1987),

$$\mu_{mix} = \frac{\sum_i \mu_i \xi_i \sqrt{MW_i}}{\sum_i \xi_i \sqrt{MW_i}}. \tag{3.28}$$

The kinematic viscosity varies by ∼3× for the range of mole fractions within the mixing layer, implying that (3.27) could vary by similar amounts. Since the average mole fraction within the mixing layer is $\xi \sim 0.5$, $\nu(\xi)$ is evaluated at this value, giving 1.60×10^{-5} m^2 s^{-1} and 1.64×10^{-5} m^2 s^{-1} for the $M = 1.6$ and $M = 2.2$ cases, respectively.

Using the length scales and (3.26), the Reynolds number grows by two orders of magnitude throughout the experiment. Using the $1/k_{2\,\%}$ value for the Batchelor scale, the turbulent transition (shown as a horizontal grey band in figure 18) is passed near the second post-shock time. A final Reynolds number of 5.7×10^4 and 7.2×10^4 is reached at the latest time in the $M = 1.6$ and $M = 2.2$ experiments, respectively. The Reynolds number based on the Batchelor scale from fitting Pope's model spectrum is considerably smaller and only predicts that the flow begins to transition to turbulence at either of the last two times ($\lambda_L/\lambda_\nu \approx 1$). These differences highlight how the uncertainty in the measurements are amplified by the power of four involved in (3.26). Since the Pope-model estimate is believed to be the upper limit of the Batchelor scale, then the corresponding curve represents the lower limit of this Reynolds number estimate. But both calculations exhibit the same trend, with a Reynolds number increasing in time due to increased scale separation as the

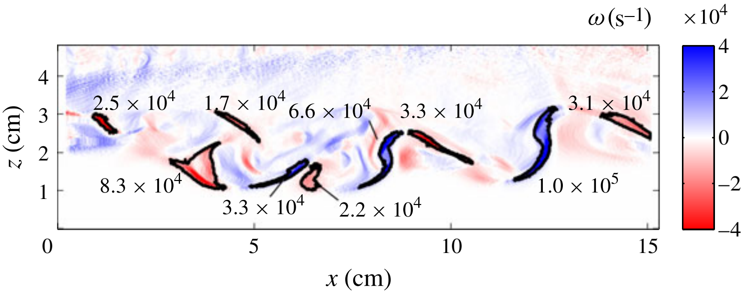

FIGURE 19. (Colour online) The estimated initial vorticity field from a $M = 1.6$ experiment. The vortex Reynolds number of several vortices are noted.

mixing layer develops. The Reynolds number using the $1/k_{2\%}$ value agrees with the conclusions of the mole fraction PDFs and the spectra, where a transition to turbulence appeared to occur near the second post-shock time. In a similar flow, Balasubramanian, Orlicz & Prestridge (2013) computed a Reynolds number based on the turbulent kinetic energy and also saw an increase in Re over time. In that case, the Reynolds number only rose by 50 %, possibly due to the flow remaining in a transitional state ($Re \approx 1.5 \times 10^4$).

The Reynolds number based on $h\dot{h}/\nu$ does not capture the transition that occurs during the experiment but is in general agreement with the final values based on λ_T/λ_B. Equation (3.27) is not expected to represent the time-dependent Reynolds number, particularly in this flow where h starts out rather large, but may represent the maximum Reynolds number that may be reached. Others (Balasubramanian *et al.* 2013; Tomkins *et al.* 2013) have noted that this definition fails to capture the ratio of inertial to viscous forces that drive RMI turbulence.

A final estimate of the Reynolds number can be made using a model of vorticity deposition on the interface and compared to the values in figure 18. Assuming an impulsive acceleration to a velocity V_0, the out-of-plane vorticity deposition on the interface is (Weber, Cook & Bonazza 2013)

$$\omega_y \approx -\frac{V_0}{\rho}\frac{\partial \rho}{\partial x}, \tag{3.29}$$

where ρ is the compressed, post-shock density field. This vorticity model is applied to a PS1, $M = 1.6$ image, which is taken immediately after shock compression where it is expected that little amplitude growth has occurred. Figure 19 shows the deposited vorticity approximation, using (3.29) and (3.12).

From figure 19, the initial post-shock layer appears to contain coherent rings and tubes of vorticity. A vortex ring in isolation becomes turbulent and breaks apart when its vortex Reynolds number is larger than 2.5×10^4 (Glezer 1988). Vortex tubes in this layer will experience similar dynamics, complicated by interactions with neighbouring vortices, thus it is appropriate to measure vortex Reynolds number within this layer. The vortex Reynolds number is defined as

$$Re_\Gamma = \frac{\Gamma}{\nu}, \tag{3.30}$$

where Γ is the circulation of the vortex core.

Vortex cores are identified in the vorticity field by isolating regions where the vorticity magnitude is above a certain threshold and integrating the vorticity, $\Gamma = \int \omega \, \mathrm{d}a$, within this region. In addition, the local viscosity is computed using the mole fraction values within the isolated region. Several vortex cores are outlined in figure 19 and their corresponding vortex Reynolds number are noted. This method finds a number of vorticity regions that are above the turbulent threshold, with a maximum of $Re_\Gamma = 1.0 \times 10^5$. This Reynolds number calculation shares similarities to the method used by Lombardini *et al.* (2012), where the impulsive RMI model of Saffman & Meiron (1989) was used to estimate the initial kinetic energy deposited on the interface and, thus, the Reynolds number. With reasonable estimates for the parameters in their model (a perturbation size of 2 cm, which is approximately the thickness of the high-variance region in figure 2(*c*), and a diffusion thickness of 4 cm, which is the compressed h_{5-95} value), a Reynolds number of 8.4×10^4 is found for this $M = 1.6$ case. These Reynolds number estimates are similar to that measured using the Taylor/Batchelor scale ratio.

Agreement between these different Reynolds number techniques is not unexpected. First, there are common roots in $h\dot{h}/\nu$ and Γ/ν. The value $h\dot{h}/\nu$ will peak between the linear and power-law stage of growth, where h is approximately equal to the dominant wavelength, λ, reaching a maximum value $\sim\lambda\dot{h}/\nu$. Through linear analysis, $\Gamma = (2/\pi)\lambda\dot{h}$ (Jacobs & Sheeley 1996). Therefore $h\dot{h}/\nu$ can be expected to peak near Γ/ν. Second, recent analysis by Tomkins *et al.* (2013) compared $h\dot{h}/\nu$, Γ/ν and locally computed values using particle-image velocimetry data, finding that these Reynolds numbers agreed within a factor of two. The Reynolds number estimate presented here based on λ_T/λ_B can be considered an additional method of estimating the local Reynolds number from PLIF data.

4. Conclusions

The turbulent mixing that results from the RMI was studied using a unique shear-layer initial condition and quantitative PLIF imaging. After acceleration by a $M = 1.6$ or $M = 2.2$ shock wave, the mixing layer is initially dominated by the growth of large-scale spikes and bubbles, but these structures eventually break apart into smaller scales, leading to molecular mixing and scale separation that is indicative of a turbulent transition. The two Mach numbers seem to evolve similarly when compared at the same interface travel distance.

The mole fraction PDFs and spectra provide evidence for turbulent mixing at late times. The PDFs show three peaks, two representing the unmixed fluids and one representing the mixed fluid that is present in the initial condition. The central peak in the PDF reduces in time and disappears by the latest time at the larger Mach number. This intermediate fluid and the light fluid are observed mixing to produce $\xi \sim 0.8$ fluid. The scalar variance energy spectra appear to be fully developed by the last two times and exhibit an inertial range close to $k^{-5/3}$.

Several length scales from within the mixing layer are measured and provide a clear picture of the scale separation that causes the turbulent transition. The large-scale extent of the mixing layer is found growing linearly early on and then as $t^{0.43}$ by the end of the experiment. The smallest length scale, the Batchelor scale, reduces from its initial condition value and reaches 100–250 μm, depending on the technique used. The intermediate scale, the Taylor microscale, shows early-time anisotropy caused by the shock wave and then stays near 4 mm for the latter three post-shock times.

The ratio of the Taylor to Batchelor scale is used to compute the Reynolds number. This Reynolds number is growing in time and crosses the turbulent transition threshold near the second post-shock time, eventually reaching 6–7 × 10^4. This result is dependent on the method used for measuring the Batchelor scale, but $\lambda_B = 1/k_{2\%}$ appears to support the results of the PDF and spectral analysis. This Reynolds number is similar to the vortex Reynolds number through an estimate of the initial baroclinic vorticity.

Acknowledgements

The authors are grateful to Dan Reese and Jose Alonso Navarro for help with the experiments and to Harry Robey for valuable feedback on this manuscript. Part of this work was performed under the auspices of the US Department of Energy by Lawrence Livermore National Laboratory under Contract DE-AC52-07NA27344. Additional support was provided to the University of Wisconsin by US DOE grant no. DE-FG52-06NA26196.

REFERENCES

Balakumar, B. J., Orlicz, G. C., Ristorcelli, J. R., Balasubramanian, S., Prestridge, K. P. & Tomkins, C. D. 2012 Turbulent mixing in a Richtmyer–Meshkov fluid layer after reshock: velocity and density statistics. *J. Fluid Mech.* **696** (410), 67–93.

Balasubramanian, S., Orlicz, G. C. & Prestridge, K. P. 2013 Experimental study of initial condition dependence on turbulent mixing in shock-accelerated Richtmyer–Meshkov fluid layers. *J. Turbul.* **14** (3), 170–196.

Banerjee, A., Kraft, W. N. & Andrews, M. J. 2010 Detailed measurements of a statistically steady Rayleigh–Taylor mixing layer from small to high Atwood numbers. *J. Fluid Mech.* **659**, 127–190.

Besnard, D., Harlow, F. H., Rauenzahn, R. M. & Zemach, C. 1992 Turbulent transport equations for variable-density turbulence and their relationship to two-field models. *Tech. Rep.* LA-12303-MA. Los Alamos National Laboratory.

Buch, K. A. & Dahm, W. J. A. 1996 Experimental study of the fine-scale structure of conserved scalar mixing in turbulent shear flows. Part 1. $Sc \gg 1$. *J. Fluid Mech.* **317**, 21–71.

Buch, K. A. & Dahm, W. J. A. 1998 Experimental study of the fine-scale structure of conserved scalar mixing in turbulent shear flows. Part 2. $Sc \sim 1$. *J. Fluid Mech.* **364**, 1–29.

Cabot, W. H. & Cook, A. W. 2006 Reynolds number effects on Rayleigh–Taylor instability with possible implications for type Ia supernovae. *Nat. Phys.* **2** (8), 562–568.

Canny, J. 1986 A computational approach to edge detection. *IEEE Trans. Pattern Anal. Mach. Intell.* **6**, 679–698.

Champagne, F. H., Harris, V. G. & Corrsin, S. 1970 Experiments on nearly homogeneous turbulent shear flow. *J. Fluid Mech.* **41** (01), 81–139.

Chisnell, R. F. 1955 The normal motion of a shock wave through a non-uniform one-dimensional medium. *Proc. R. Soc. Lond.* A **232** (1190), 350–370.

Clemens, N. T. 2002 Flow imaging. In *Encyclopedia of Imaging Science and Technology* (ed. J. P. Hornak), pp. 390–420. John Wiley and Sons.

Collins, B. D. & Jacobs, J. W. 2002 PLIF flow visualization and measurements of the Richtmyer–Meshkov instability of an air/SF6 interface. *J. Fluid Mech.* **464**, 113–136.

Cook, A. W., Cabot, W. & Miller, P. L. 2004 The mixing transition in Rayleigh–Taylor instability. *J. Fluid Mech.* **511**, 333–362.

Cook, A. W. & Dimotakis, P. E. 2001 Transition stages of Rayleigh–Taylor instability between miscible fluids. *J. Fluid Mech.* **443**, 69–99.

Dimonte, G. & Schneider, M. 1997 Turbulent Richtmyer–Meshkov instability experiments with strong radiatively driven shocks. *Phys. Plasmas* **4** (12), 4347–4357.

Dimonte, G. & Schneider, M. 2000 Density ratio dependence of Rayleigh–Taylor mixing for sustained and impulsive acceleration histories. *Phys. Fluids* **12**, 304–321.

DIMOTAKIS, P. E. 2000 The mixing transition in turbulent flows. *J. Fluid Mech.* **409**, 69–98.

DIMOTAKIS, P. E., CATRAKIS, H. J. & FOURGUETTE, D. C. 2001 Flow structure and optical beam propagation in high-Reynolds-number gas-phase shear layers and jets. *J. Fluid Mech.* **433**, 105–134.

GHANDHI, J. B. 2006 Spatial resolution and noise considerations in determining scalar dissipation rate from passive scalar image data. *Exp. Fluids* **40**, 577–588.

GLEZER, A. 1988 The formation of vortex rings. *Phys. Fluids* **31**, 3532–3542.

GRÉGOIRE, O., SOUFFLAND, D. & GAUTHIER, S. 2005 A second-order turbulence model for gaseous mixtures induced by Richtmyer–Meshkov instability. *J. Turbul.* **6**, N29.

JACOBS, J. W., KRIVETS, V. V., TSIKLASHVILI, V. & LIKHACHEV, O. A. 2013 Experiments on the Richtmyer–Meshkov instability with an imposed, random initial perturbation. *Shock Waves* **23** (4), 407–413.

JACOBS, J. W. & SHEELEY, J. M. 1996 Experimental study of incompressible Richtmyer–Meshkov instability. *Phys. Fluids* **8** (2), 405–415.

JONES, M. A. & JACOBS, J. W. 1997 A membraneless experiment for the study of Richtmyer–Meshkov instability of a shock-accelerated gas interface. *Phys. Fluids* **9** (10), 3078–3085.

KAISER, S. A. & FRANK, J. H. 2007 Imaging of dissipative structures in the near field of a turbulent non-premixed jet flame. *Proc. Combust. Inst.* **31** (1), 1515–1523.

KAISER, S. A. & FRANK, J. H. 2011 The effects of laser-sheet thickness on dissipation measurements in turbulent non-reacting jets and jet flames. *Meas. Sci. Technol.* **22** (4), 045403.

KANE, J., DRAKE, R. P. & REMINGTON, B. A. 1999 An evaluation of the Richtmyer–Meshkov instability in supernova remnant formation. *Astrophys. J.* **511** (1), 335–340.

LEINOV, E., MALAMUD, G., ELBAZ, Y., LEVIN, L. A., BEN-DOR, G., SHVARTS, D. & SADOT, O. 2009 Experimental and numerical investigation of the Richtmyer–Meshkov instability under re-shock conditions. *J. Fluid Mech.* **626**, 449–475.

LINDL, J. D., AMENDT, P., BERGER, R. L., GLENDINNING, S. G., GLENZER, S. H., HAAN, S. W., KAUFFMAN, R. L., LANDEN, O. L. & SUTER, L. J. 2004 The physics basis for ignition using indirect-drive targets on the national ignition facility. *Phys. Plasmas* **11** (2), 339–491.

LIVESCU, D. & RISTORCELLI, J. R. 2008 Variable-density mixing in buoyancy-driven turbulence. *J. Fluid Mech.* **605**, 145–180.

LIVESCU, D., RISTORCELLI, J. R., GORE, R. A., DEAN, S. H., CABOT, W. H. & COOK, A. W. 2009 High-Reynolds number Rayleigh–Taylor turbulence. *J. Turbul.* **10** (13), 1–32.

LOMBARDINI, M., PULLIN, D. I. & MEIRON, D. I. 2012 Transition to turbulence in shock-driven mixing: a Mach number study. *J. Fluid Mech.* **690**, 203–226.

MARBLE, F., HENDRICKS, G. & ZUKOSKI, E. 1987 Progress toward shock enhancement of supersonic combustion processes. In *23rd AIAA, SAE, ASME, and ASEE, Joint Propulsion Conference, San Diego, CA, June 29–July 2,* American Institute of Aeronautics and Astronautics, New York, pp. 1–8.

MESHKOV, E. E. 1970 Instability of a shock wave accelerated interface between two gases. *NASA Tech. Transl.* **13**, 1–14.

MIKAELIAN, K. 1989 Turbulent mixing generated by Rayleigh–Taylor and Richtmyer–Meshkov instabilities. *Physica* D **36**, 343–357.

MOTL, B., OAKLEY, J., RANJAN, D., WEBER, C., ANDERSON, M. & BONAZZA, R. 2009 Experimental validation of a Richtmyer–Meshkov scaling law over large density ratio and shock strength ranges. *Phys. Fluids* **21** (12), 126102.

ORLICZ, G. C., BALAKUMAR, B. J., TOMKINS, C. D. & PRESTRIDGE, K. P. 2009 A Mach number study of the Richtmyer–Meshkov instability in a varicose, heavy-gas curtain. *Phys. Fluids* **21** (6), 064102.

ORLICZ, G. C., BALASUBRAMANIAN, S. & PRESTRIDGE, K. P. 2013 Incident shock Mach number effects on Richtmyer–Meshkov mixing in a heavy gas layer. *Phys. Fluids* **25** (11), 114101.

PETERSEN, B. & GHANDHI, J. 2011 High-resolution turbulent scalar field measurements in an optically accessible internal combustion engine. *Exp. Fluids* **51**, 1695–1708.

POPE, S. 2000 *Turbulent Flows*. Cambridge University Press.

Prasad, J. K., Rasheed, A., Kumar, S. & Sturtevant, B. 2000 The late-time development of the Richtmyer–Meshkov instability. *Phys. Fluids* **12** (8), 2108–2115.

Ramaprabhu, P. & Andrews, M. J. 2004 Experimental investigation of Rayleigh–Taylor mixing at small Atwood numbers. *J. Fluid Mech.* **502**, 233–271.

Ranjan, D., Oakley, J. & Bonazza, R. 2011 Shock-bubble interactions. *Annu. Rev. Fluid Mech.* **43**, 117–140.

Rayleigh, L. 1883 Investigation of the character of the equilibrium of an incompressible heavy fluid of variable density. *Proc. Lond. Math. Soc.* **14** (1), 170–177.

Read, K. I. 1984 Experimental investigation of turbulent mixing by Rayleigh–Taylor instability. *Physica* D **12** (1–3), 45–58.

Reid, R. C., Prausnitz, J. M. & Poling, B. E. 1987 *The Properties of Gases and Liquids*. McGraw-Hill.

Richtmyer, R. D. 1960 Taylor instability in shock acceleration of compressible fluids. *Commun. Pure Appl. Maths* **13** (2), 297–319.

Rightley, P. M., Vorobieff, P., Martin, R. & Benjamin, R. F. 1999 Experimental observations of the mixing transition in a shock-accelerated gas curtain. *Phys. Fluids* **11** (1), 186–200.

Ristorcelli, J. R. & Clark, T. T. 2004 Rayleigh–Taylor turbulence: self-similar analysis and direct numerical simulations. *J. Fluid Mech.* **507**, 213–253.

Ristorcelli, J. R., Gowardhan, A. A. & Grinstein, F. F. 2013 Two classes of Richtmyer–Meshkov instabilities: a detailed statistical look. *Phys. Fluids* **25** (4), 044106.

Robey, H. F., Zhou, Y., Buckingham, A. C., Keiter, P., Remington, B. A. & Drake, R. P. 2003 The time scale for the transition to turbulence in a high Reynolds number, accelerated flow. *Phys. Plasmas* **10** (3), 614–622.

Saffman, P. G. & Meiron, D. I. 1989 Kinetic energy generated by the incompressible Richtmyer–Meshkov instability in a continuously stratified fluid. *Phys. Fluids* A **1** (11), 1767–1771.

Su, L. K. & Clemens, N. T. 2003 The structure of fine-scale scalar mixing in gas-phase planar turbulent jets. *J. Fluid Mech.* **488**, 1–29.

Taylor, G. 1950 The instability of liquid surfaces when accelerated in a direction perpendicular to their planes. I. *Proc. R. Soc. Lond.* **201** (1065), 192–196.

Tennekes, H. & Lumley, J. L. 1972 *A First Course in Turbulence*. The MIT Press.

Tomkins, C. D., Balakumar, B. J., Orlicz, G., Prestridge, K. P. & Ristorcelli, J. R. 2013 Evolution of the density self-correlation in developing Richtmyer–Meshkov turbulence. *J. Fluid Mech.* **735**, 288–306.

Tomkins, C., Kumar, S., Orlicz, G. & Prestridge, K. 2008 An experimental investigation of mixing mechanisms in shock-accelerated flow. *J. Fluid Mech.* **611**, 131–150.

Vetter, M. & Sturtevant, B. 1995 Experiments on the Richtmyer–Meshkov instability of an air/SF_6 interface. *Shock Waves* **4**, 247–252.

Vorobieff, P., Mohamed, N. G., Tomkins, C., Goodenough, C., Marr-Lyon, M. & Benjamin, R. F. 2003 Scaling evolution in shock-induced transition to turbulence. *Phys. Rev.* E **68** (6), 065301.

Vorobieff, P., Rightley, P. M. & Benjamin, R. F. 1998 Power-law spectra of incipient gas-curtain turbulence. *Phys. Rev. Lett.* **81**, 2240–2243.

Wang, G. H. & Clemens, N. T. 2004 Effects of imaging system blur on measurements of flow scalars and scalar gradients. *Exp. Fluids* **37** (2), 194–205.

Wang, G. H., Clemens, N. T., Barlow, R. S. & Varghese, P. L. 2007 A system model for assessing scalar dissipation measurement accuracy in turbulent flows. *Meas. Sci. Technol.* **18**, 1287–1303.

Weber, C. R. 2012 Turbulent mixing measurements in the Richtmyer–Meshkov instability. PhD thesis, University of Wisconsin–Madison.

Weber, C. R., Cook, A. W. & Bonazza, R. 2013 Growth rate of a shocked mixing layer with known initial perturbations. *J. Fluid Mech.* **725**, 372–401.

Weber, C. R., Haehn, N., Oakley, J., Rothamer, D. & Bonazza, R. 2012 Turbulent mixing measurements in the Richtmyer–Meshkov instability. *Phys. Fluids* **24** (7), 074105.

YOUNGS, D. L. 1984 Numerical simulation of turbulent mixing by Rayleigh–Taylor instability. *Physica* D **12** (1–3), 32–44.

ZHOU, Y., ROBEY, H. & BUCKINGHAM, A. 2003 Onset of turbulence in accelerated high-Reynolds-number flow. *Phys. Rev.* E **67** (5), 056305.